



ARL-SR-0337 • SEP 2015



Flight Behaviors of a Complex Projectile Using a Coupled Computational Fluid Dynamics (CFD)-based Simulation Technique: Free Motion

by Jubaraj Sahu and Frank Fresconi

Approved for public release; distribution is unlimited.

NOTICES

Disclaimers

The findings in this report are not to be construed as an official Department of the Army position unless so designated by other authorized documents.

Citation of manufacturer's or trade names does not constitute an official endorsement or approval of the use thereof.

Destroy this report when it is no longer needed. Do not return it to the originator.



Flight Behaviors of a Complex Projectile Using a Coupled Computational Fluid Dynamics (CFD)-based Simulation Technique: Free Motion

by Jubaraj Sahu and Frank Fresconi

Weapons and Materials Research Directorate, ARL

REPORT DOCUMENTATION PAGE				Form Approved OMB No. 0704-0188	
<p>Public reporting burden for this collection of information is estimated to average 1 hour per response, including the time for reviewing instructions, searching existing data sources, gathering and maintaining the data needed, and completing and reviewing the collection information. Send comments regarding this burden estimate or any other aspect of this collection of information, including suggestions for reducing the burden, to Department of Defense, Washington Headquarters Services, Directorate for Information Operations and Reports (0704-0188), 1215 Jefferson Davis Highway, Suite 1204, Arlington, VA 22202-4302. Respondents should be aware that notwithstanding any other provision of law, no person shall be subject to any penalty for failing to comply with a collection of information if it does not display a currently valid OMB control number.</p> <p>PLEASE DO NOT RETURN YOUR FORM TO THE ABOVE ADDRESS.</p>					
1. REPORT DATE (DD-MM-YYYY) September 2015		2. REPORT TYPE Final		3. DATES COVERED (From - To) October 2014–May 2015	
4. TITLE AND SUBTITLE Flight Behaviors of a Complex Projectile Using a Coupled Computational Fluid Dynamics (CFD)-based Simulation Technique: Free Motion				5a. CONTRACT NUMBER	
				5b. GRANT NUMBER	
				5c. PROGRAM ELEMENT NUMBER	
6. AUTHOR(S) Jubaraj Sahu and Frank Fresconi				5d. PROJECT NUMBER AH80	
				5e. TASK NUMBER	
				5f. WORK UNIT NUMBER	
7. PERFORMING ORGANIZATION NAME(S) AND ADDRESS(ES) US Army Research Laboratory ATTN: RDRL-WML-E Aberdeen Proving Ground, MD 21005-5069				8. PERFORMING ORGANIZATION REPORT NUMBER ARL-SR-0337	
9. SPONSORING/MONITORING AGENCY NAME(S) AND ADDRESS(ES)				10. SPONSOR/MONITOR'S ACRONYM(S)	
				11. SPONSOR/MONITOR'S REPORT NUMBER(S)	
12. DISTRIBUTION/AVAILABILITY STATEMENT Approved for public release; distribution is unlimited.					
13. SUPPLEMENTARY NOTES					
14. ABSTRACT <p>This report describes a computational study to understand the free roll, pitch, and yaw motion of a canard-controlled, fin-stabilized projectile. Numerical computations were performed for this projectile using an advanced coupled computational fluid dynamics and rigid body dynamics technique. Additionally, the coupled approach was tailored to be constraints-based for the rigid body dynamics allowing for pure pitching and pure rolling motions to be studied prior to considering the full roll-pitch-yaw motion. Flow visualizations and aerodynamic force and moment computations indicate unsteady canard stall at high angle of attack and significant interaction of these canard vortices on the afterbody-fins. Parameter estimation was performed to obtain aerodynamic coefficients, assess the aerodynamic model, and understand the roll-pitch-yaw coupling. These results suggest that improvements to aerodynamic modeling are necessary to better capture high angle-of-attack phenomenon such as unsteady canard stall and vortex interactions. Analysis of the pure pitch and pure roll predicts the coupled roll-pitch-yaw motion well with the exception of unsteady and interaction effects during periods of high angle of attack.</p>					
15. SUBJECT TERMS coupled method, virtual fly-out, pitch, roll-pitch-yaw motion, parameter estimation					
16. SECURITY CLASSIFICATION OF:			17. LIMITATION OF ABSTRACT UU	18. NUMBER OF PAGES 52	19a. NAME OF RESPONSIBLE PERSON Jubaraj Sahu
a. REPORT Unclassified	b. ABSTRACT Unclassified	c. THIS PAGE Unclassified			19b. TELEPHONE NUMBER (Include area code) 410-306-0798

Contents

List of Figures	iv
List of Tables	v
Preface	vi
Acknowledgments	vii
1. Introduction	1
2. Computational Methodology	3
3. Coupled CFD/RBD Approach	4
4. Aerodynamics Modeling	5
5. Model Geometry and Grid	9
6. Results	11
6.1 Pure Pitching Case	17
6.2 Pure Rolling Case	24
6.3 Roll-Pitch-Yaw Case	26
7. Conclusions	31
8. References	33
Appendix. Aerodynamic Coefficients at Mach 0.6	37
List of Symbols, Abbreviations, Acronyms, and Nomenclature	39
Distribution List	41

List of Figures

Fig. 1	Body-fixed coordinate system and aerodynamic angles.....	5
Fig. 2	Computational model of the projectile geometry	9
Fig. 3	Expanded view of the mesh in the XZ plane near the body	10
Fig. 4	View of the mesh in the circumferential plane, near the canard before overset	10
Fig. 5	View of the mesh in the circumferential plane, near the canards after overset cut	11
Fig. 6	Particle traces at 3 different instants in time during roll-pitch-yaw motion, $M = 0.6$, (a) $t = 0.03$, (b) $t = 0.15$, and (c) $t = 0.26$ s	13
Fig. 7	Vorticity contours at different instants in time during initial phase of roll-pitch-yaw motion, $M = 0.6$, $0.02 \leq t \leq 0.07$ s	14
Fig. 8	Surface pressure contours at different instants in time during initial phase of roll-pitch-yaw motion, $M = 0.6$, $0.02 \leq t \leq 0.07$ s	16
Fig. 9	Expanded view of surface pressure contours near the fins at different instants in time during initial phase of roll-pitch-yaw motion, $M = 0.6$, $0.02 \leq t \leq 0.07$ s	17
Fig. 10	Euler pitch angle (left) and pitch rate (right) for pure pitching case ...	17
Fig. 11	Axial force coefficient of body-fin (top left), normal force coefficient of body-fin (top right), roll moment coefficient of body-fin (middle left), pitching moment coefficient of body-fin (middle right), and side moment of body-fin (bottom) from pure pitching motion	19
Fig. 12	Axial force coefficient of canard (top left), normal force coefficient of canard (top right), roll moment coefficient of canard (bottom left), and pitching moment coefficient of canard (bottom right) from pure pitching	20
Fig. 13	States from parameter estimation analysis of pure pitching (Euler pitch angle root-sum-square fit error 0.15°)	22
Fig. 14	Pitching moments from parameter estimation analysis for pure pitching (top left = body-fin, top right = individual canard, bottom = total)	23
Fig. 15	States from parameter estimation analysis of pure rolling (Euler roll angle root-sum-square fit error 0.1°)	24
Fig. 16	Rolling moments from parameter estimation analysis for pure rolling (top left = body-fin, top right = individual canard, bottom = total)	25
Fig. 17	Axial force coefficient of body-fin (top left), normal force coefficient of body-fin (top right), roll moment coefficient of body-fin (bottom left), and pitching moment coefficient of body-fin (bottom right) from roll-pitch-yaw motion	26

Fig. 18	Axial force coefficient of canard (top left), normal force coefficient of canard (top right), roll moment coefficient of canard (bottom left), and pitching moment coefficient of canard (bottom right) from roll-pitch-yaw motion.....	27
Fig. 19	Euler roll (top left), pitch (top right), and yaw (bottom) angles from parameter estimation analysis of roll-pitch-yaw (root-sum-square fit errors of 0.32° , 0.19° , and 0.19° in Euler roll, pitch, and yaw angles) 28	
Fig. 20	Roll (top left), pitch (top right), and yaw (bottom) rates from parameter estimation analysis of roll-pitch-yaw	29
Fig. 21	Total moments from parameter estimation analysis for roll-pitch-yaw (top left = roll, top right = pitch, bottom = yaw)	30
Fig. 22	Rolling moment coefficient of body-fin (top left), pitching moment coefficient of body-fin (top right), side moment coefficient of body-fin (middle), rolling moment coefficient of canard (bottom left), and pitching moment coefficient of canard (bottom right) from direct method and parameter estimation of roll-pitch-yaw	31

List of Tables

Table 1	Initial conditions for coupled simulations.....	12
Table 2	Aerodynamic coefficients for body-fin at Mach 0.6 from direct analysis of pure pitching	21
Table 3	Aerodynamic coefficients for canard at Mach 0.6 from direct analysis of pure pitching	21
Table 4	Aerodynamic coefficients at Mach 0.6 from parameter estimation of pure pitching, $C_{mq} = -80.7$	24
Table 5	Aerodynamic coefficients at Mach 0.6 from parameter estimation of pure rolling, $C_{lp} = -12.1$	25
Table A-1	Aerodynamic coefficients at Mach 0.6 from direct and parameter estimation analysis of roll-pitch-yaw	38

Preface

The paper “Flight Behaviors of a Complex Projectile using a Coupled CFD-based Simulation Technique: Free Motion” was originally published in *Proceedings of the 33rd AIAA Applied Aerodynamics Conference* (2015 June 22–26, Dallas, TX). This version contains a few important minor modifications of the original publication based on additional reviews.

Acknowledgments

This work was accomplished as part of a grand challenge project jointly sponsored by the Department of Defense High Performance Computing Modernization program and the US Army Research Laboratory. The author also wishes to thank Dr Sidra Siltan and Ms Karen R Heavey for their help with the computational meshes, Dr Sukumar Chakravarthy of Metacomp Technologies for providing expert advice on the coupled simulations, and Mr Richard Angelini for his help with advanced flow visualizations.

INTENTIONALLY LEFT BLANK.

1. Introduction

Accurate determination of flight behaviors is critical to the development of new, affordable munitions. Various techniques such as the semiempirical,^{1,2} wind tunnel,^{3,4} free-flight,⁵⁻⁷ and computational fluid dynamics (CFD).⁸⁻¹⁰ are used routinely for aerodynamic characterization of projectiles. Rigid body flight dynamics often utilize aerodynamic coefficients obtained using these techniques within an aerodynamic model framework. A major concern, especially when adding moveable aerodynamic surfaces (MAS) (e.g., canards) upstream of the body or stabilizing fins, is flow interactions.^{11,12} The motion of upstream control surfaces at various aerodynamic angles of attack and Mach numbers greatly influences the pressure distribution on downstream surfaces. Even for unguided flights, these flow interactions exist and must be accurately taken into account in the design analysis. A significant contribution to these studies would be shifting from multidimensional table look-ups based on exhaustive aerodynamic quantification to mathematical models that inherently include effects captured in the multidimensional tables.

Fortunately, improved computer technology and state-of-the-art numerical procedures have continued to enable solutions to complex, 3-dimensional (3-D) problems associated with projectile and missile aerodynamics.^{8-10,12-14} In particular, CFD has become a powerful tool for the prediction of aerodynamics and for subsequent design and performance evaluation of these weapon systems. It is essential that CFD be brought into the earlier stages of design and development to be more effective. Our recent focus has therefore been directed at the development and application of advanced predictive capabilities to compute the unsteady aerodynamics of both unguided and guided projectiles at all speeds from subsonic to supersonic speeds. Accurate numerical modeling of the unsteady aerodynamics has been found to be challenging and has required the use of time-accurate solutions techniques.

New advanced computational techniques are being developed to understand flight behaviors of both unguided and guided projectiles. One such technique involves coupling of CFD and rigid body dynamics (RBD) codes for the simulation of projectile free flight motion in a time-accurate manner. This technique, known as coupled CFD/RBD or virtual fly-out method,¹⁵ uses advanced CFD methods to characterize the unsteady aerodynamics at each instant in time during flight. In the coupled CFD/RBD procedure, the aerodynamic forces and moments are computed at every time step in the CFD solver and transferred to the RBD code. The RBD code computes the projectile body's response to the forces and moments. The

output of RBD state variables are transferred back to the CFD flow solver, which then computes the aerodynamic forces and moments at the next time step subject to the updated RBD states. This process marches forward in time from a given set of initial conditions for the fly-out simulations. This coupled technique provides both the unsteady aerodynamics and the flight dynamics in an integrated manner. It yields a wealth of data unavailable in experimental methods, but it does involve highly computer-intensive calculations requiring large computational resources. Flow fields, pressure distributions (and hence forces and moments) on various surfaces, and the complete 12-state RBD history are available from the coupled solutions. The coupled CFD/RBD technique has already been demonstrated for various finned- and spin-stabilized projectiles^{16–20} and validated in some of these cases. Computed results obtained from the coupled simulations were validated with available free-flight test data at subsonic, transonic, and supersonic speeds. This technique was further extended for computation of free-flight aerodynamics and flight dynamics of a finned projectile with pulse jet control²¹ and is being extended for guided flights.^{22,23}

The approach for coupled CFD/RBD simulations is to capture static and dynamic aerodynamic behavior over short time durations with different motions. Coupling the flight dynamics with the fluid mechanics helps ensure that the data are collected over the appropriate conditions (e.g., angle of attack, angular rate). Ultimately, this method obtains aerodynamic data and enables aerodynamic models to be built and verified. Performing coupled simulations in this manner allows for screening of situations where conventional aerodynamic models based on static wind tunnel or CFD techniques break down. These instances are encountered more often as wider classes of munitions (small-medium-large caliber) feature control inputs and the associated flow complexity such as interactions, unsteadiness, and high angle of attack. Thus, a major benefit of these coupled simulations is to mitigate risk of unanticipated flight behaviors during guided, free-flight experiments.

Of particular interest are investigations into flight motions such as the pure pitch, pure rolling motion, and a complex roll-pitch-yaw motion. Constraints-based coupled fly-out simulation approaches have been developed in this research to generate aerodynamics for pure pitch, pure roll, and coupled roll-pitch-yaw dynamics with free motion (no control input). The novel contributions of this study include using coupled techniques on high maneuverability airframes to identify high angle-of-attack effects, evaluating aerodynamic modeling performance, and assessing the significance of coupling between degrees of freedom (DOF). This report details the constraints-based coupled CFD/RBD technique, which is applied to a highly maneuverable, canard-controlled, fin-stabilized projectile design to

facilitate complete flight analysis. The following sections describe the CFD method used, coupled numerical procedure, aerodynamic modeling, and computed results obtained for various flight motions.

2. Computational Methodology

Time-accurate, coupled CFD/RBD computations were performed using Navier-Stokes techniques for a canard-controlled projectile at Mach, $M = 0.6$. Both unsteady aerodynamics and flight dynamics were computed simultaneously and the flight response of the projectile was determined. In all cases, full 3-D solutions were obtained and no symmetry was used.

The complete set of 3-D time-dependent Navier-Stokes equations is solved in a time-asymptote manner to obtain converged steady-state solutions. A commercially available code, CFD++,^{24,25} is used and the 3-D, time-dependent Reynolds-averaged Navier-Stokes equations are solved using the following finite volume method:

$$\frac{\partial}{\partial t} \int_V \mathbf{W} dV + \oint [\mathbf{F} - \mathbf{G}] \cdot d\mathbf{A} = \int_V \mathbf{H} dV \quad (1)$$

where \mathbf{W} is the vector of conservative variables, \mathbf{F} and \mathbf{G} are the inviscid and viscous flux vectors, respectively, \mathbf{H} is the vector of source terms, V is the cell volume, and A is the surface area of the cell face.

Several techniques such as implicit scheme and relaxation are used to achieve faster convergence. Use of an implicit scheme circumvents the stringent stability limits suffered by their explicit counterparts, and successive relaxation allows update of cells as information becomes available and thus aids convergence. Second-order discretization was used for the flow variables and the turbulent viscosity equation. The turbulence closure is based on topology-parameter-free formulations. A realizable 2-equation k - ϵ turbulence model²⁶ was used for the computation of turbulent flows. These models are ideally suited to unstructured bookkeeping and massively parallel processing due to their independence from constraints related to the placement of boundaries and/or zonal interfaces. The basic CFD solution technique described here is coupled with RBD for simultaneous prediction of both uncontrolled and control flights.

3. Coupled CFD/RBD Approach

Research efforts are ongoing to perform time-accurate multidisciplinary coupled CFD/RBD computations for complex guided projectiles. With or without flight control, the coupled CFD/RBD procedure allows 1) “virtual fly-out” of projectiles on the supercomputers and 2) the prediction of actual flight paths of a projectile and all the associated unsteady free-flight aerodynamics in an integrated manner. A time-accurate numerical approach is used in the coupled virtual fly-out simulations. This approach requires that the 6DOF body dynamics be computed at each repetition of a flow solver. The CFD capability used here solves the same Navier-Stokes equations shown in Eq. 1 and incorporates advanced boundary conditions and grid motion capabilities. For time-accurate simulations of virtual fly-outs that are of interest here, a dual time-stepping procedure was used to achieve the desired time accuracy in the time-accurate solutions. The whole grid was moved to take into account the motion of the projectile. To account for RBD, the grid point velocities were set as if the grid is attached to the rigid body with 6DOF.

The 6DOF model for the projectile flight is shown in Eq. 2.

$$\begin{aligned}
 \begin{bmatrix} \dot{x} \\ \dot{y} \\ \dot{z} \end{bmatrix} &= \begin{bmatrix} c_\theta c_\psi & s_\phi s_\theta c_\psi - c_\phi s_\psi & c_\phi s_\theta c_\psi + s_\phi s_\psi \\ c_\theta s_\psi & s_\phi s_\theta s_\psi + c_\phi c_\psi & c_\phi s_\theta s_\psi + s_\phi c_\psi \\ -s_\theta & s_\phi c_\theta & c_\phi c_\theta \end{bmatrix} \begin{bmatrix} u \\ v \\ w \end{bmatrix} \\
 \begin{bmatrix} \dot{\phi} \\ \dot{\theta} \\ \dot{\psi} \end{bmatrix} &= \begin{bmatrix} 1 & s_\phi t_\theta & c_\phi t_\theta \\ 0 & c_\phi & -s_\phi \\ 0 & s_\phi/c_\theta & c_\phi/c_\theta \end{bmatrix} \begin{bmatrix} p \\ q \\ r \end{bmatrix} \\
 \begin{bmatrix} \dot{u} \\ \dot{v} \\ \dot{w} \end{bmatrix} &= \frac{1}{m} \begin{bmatrix} X \\ Y \\ Z \end{bmatrix} - \begin{bmatrix} 0 & -r & q \\ r & 0 & -p \\ -q & p & 0 \end{bmatrix} \begin{bmatrix} u \\ v \\ w \end{bmatrix} \\
 \begin{bmatrix} \dot{p} \\ \dot{q} \\ \dot{r} \end{bmatrix} &= \tilde{I}^{-1} \begin{bmatrix} L \\ M \\ N \end{bmatrix} - \tilde{I}^{-1} \begin{bmatrix} 0 & -r & q \\ r & 0 & -p \\ -q & p & 0 \end{bmatrix} \tilde{I} \begin{bmatrix} p \\ q \\ r \end{bmatrix}
 \end{aligned} \tag{2}$$

These equations are numerically integrated forward in time to obtain the flight dynamic response. The dynamics are constrained by setting certain moments or forces to zero depending on the dynamics being isolated, hence the term “constraints-based”. As an example, when examining the pitch-only motion at a specific Mach number, all forces and the roll and yaw moments are set to zero.

Typically, the coupled solution procedure requires 3 steps. First, we begin with a computation performed in the “steady-state mode” with the grid velocities prescribed to account only for the translational motion component of the complete set of initial conditions. At the second step, we also impose the angular orientations

from the initial conditions and spin rate is added for spinning projectiles. Computations are performed with the spin in a time-accurate mode for a desired number of spin cycles. Converged solution from this second step provides the initial condition for the third step. In the third step, the remaining rotational velocity components (pitch and yaw) are added and a completely coupled CFD/RBD computation is performed in time-accurate mode. The solution from the third step should correspond to the complete set of initial conditions that includes all translational and rotational velocity components and accounts for initial position and angular orientations.

4. Aerodynamics Modeling

The aerodynamic model relates the aerodynamic data to the aerodynamic forces and moments acting on a projectile in flight. Aerodynamic data, in the form of coefficients, reduce the complex fluid mechanics around the projectile to a form amenable to analysis. Aerodynamic characterization techniques (semiempirical aeroprediction, wind tunnel, CFD, spark range, onboard sensor) yield forces and moments in the body frame.

An illustration of the projectile with the body-fixed coordinate system (Fig. 1) permits definition of the sense of forces and moments and aerodynamic angles.

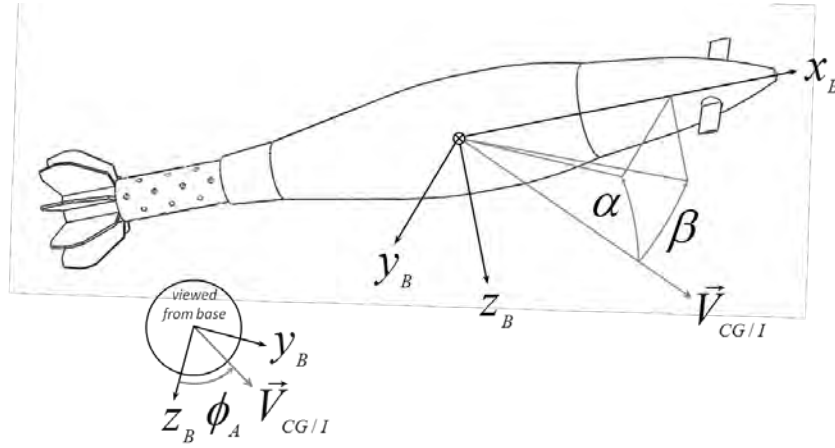


Fig. 1 Body-fixed coordinate system and aerodynamic angles

Aerodynamic angles are computed based on the body-fixed velocity components. The pitch angle of attack (or sometimes just angle of attack) is defined as

$$\alpha = \arcsin \left[\frac{w}{\sqrt{u^2 + v^2 + w^2}} \right] \quad (4)$$

The yaw angle of attack (or sometimes sideslip angle) is

$$\beta = \arcsin \left[\frac{v}{\sqrt{u^2 + v^2 + w^2}} \right] \quad (5)$$

The aerodynamic roll angle is

$$\phi_A = \arctan \left[\frac{v}{w} \right] \quad (6)$$

Finally, the total angle of attack is the root-square-sum of the pitch and yaw angles of attack:

$$\bar{\alpha} = \sqrt{\alpha^2 + \beta^2} \quad (7)$$

Total aerodynamic forces and moments are separated into rigid (i.e., body-fin surfaces in this report) and MAS (i.e., canard surfaces in this report). Rigid aerodynamic surface (RAS) forces include static (linear and nonlinear) and dynamic terms. Symbols in parenthesis indicate functional form of aerodynamic coefficients. The dynamic pressure is $Q = \frac{1}{2} \rho V^2$ and aerodynamic reference area is $S = \frac{\pi}{4} D^2$, where D is the projectile diameter and V is the total velocity.

$$\begin{aligned} X_R = -QS & \left[C_{X_0}(M) + C_{X_{\bar{\alpha}}}(M) \sin \bar{\alpha} + C_{X_{\bar{\alpha}^2}}(M) \sin^2 \bar{\alpha} \right. \\ & \left. + C_{X_{\bar{\alpha}^3}}(M) \sin^3 \bar{\alpha} + C_{X_{\bar{\alpha}^4}}(M) \sin^4 \bar{\alpha} \right] \end{aligned} \quad (8)$$

$$\begin{aligned} Y_R = -QS & \left[C_{Y_0}(M) + C_{Y_{\beta}}(M) \sin \beta + C_{Y_{\beta^3}}(M) \sin^3 \beta \right. \\ & \left. + C_{Y_{\beta^5}}(M) \sin^5 \beta \right] \end{aligned} \quad (9)$$

$$\begin{aligned} Z_R = -QS & \left[C_{Z_0}(M) + C_{Z_{\alpha}}(M) \sin \alpha + C_{Z_{\alpha^3}}(M) \sin^3 \alpha \right. \\ & \left. + C_{Z_{\alpha^5}}(M) \sin^5 \alpha \right] \end{aligned} \quad (10)$$

RAS moments also include static (linear and nonlinear) and dynamic terms. The pitching moment accounts for a center-of-gravity (CG_N), which has been shifted from the center of gravity ($CG_{N,A}$) used to obtain the aerodynamic data. The center of gravity is measured from the nose and is given in units of calibers.

$$\begin{aligned} L_R = QSD & \left[C_{l_0}(M) + C_{l_{\bar{\alpha}}}(M) \sin \bar{\alpha} + C_{l_{\bar{\alpha}^2}}(M) \sin^2 \bar{\alpha} \right. \\ & \left. + C_{l_{\bar{\alpha}^3}}(M) \sin^3 \bar{\alpha} + C_{l_{\bar{\alpha}^4}}(M) \sin^4 \bar{\alpha} \right. \\ & \left. + C_{l_p}(M) \frac{pD}{2V} \right] \end{aligned} \quad (11)$$

$$\begin{aligned}
M_R = QSD \left[C_{m_0}(M) + C_{m_\alpha}(M) \sin \alpha + C_{m_{\alpha^3}}(M) \sin^3 \alpha \right. \\
\left. + C_{m_{\alpha^5}}(M) \sin^5 \alpha + C_{m_q}(M) \frac{qD}{2V} \right] \\
- Z_R(CG_N - CG_{N,A})D
\end{aligned} \tag{12}$$

$$\begin{aligned}
N_R = QSD \left[-C_{n_0}(M) - C_{n_\beta}(M) \sin \beta - C_{n_{\beta^3}}(M) \sin^3 \beta \right. \\
\left. - C_{n_{\beta^5}}(M) \sin^5 \beta + C_{m_r}(M) \frac{rD}{2V} \right] \\
+ Y_R(CG_N - CG_{N,A})D
\end{aligned} \tag{13}$$

The following approach may be used to calculate MAS forces and moments for the i th blade. First, compute local velocity at each blade from center-of-pressure data (CP, measured in calibers forward of CG), blade geometry (ϕ_{M_i}), and rigid-body states using the equation relating the velocity of 2 fixed points on a rigid body.

$$\vec{V}_{M_i/I} = \vec{V}_{CG/I} + \vec{\omega}_{B/I} \times \vec{r}_{CG \rightarrow CP_i} \tag{14}$$

where $\vec{V}_{CG/I} = [u \ v \ w]^T$, $\vec{\omega}_{B/I} = [p \ q \ r]^T$, and $\vec{r}_{CG \rightarrow CP_i} = D[(CP_X(M, \delta_{C_i}) + CG_N - CG_{N,A}) \ CP_R \cos(\phi_{M_i}) \ CP_R \sin(\phi_{M_i})]^T$. The axial and radial center of pressure of the MAS is a function of Mach number and lifting surface deflection angle δ_i .

Obtain local velocity at each blade in the blade coordinate system using the transformation matrix:

$$\vec{T}_{BM_i} = \begin{bmatrix} 1 & 0 & 0 \\ 0 & \cos(\phi_{M_i}) & \sin(\phi_{M_i}) \\ 0 & -\sin(\phi_{M_i}) & \cos(\phi_{M_i}) \end{bmatrix} \tag{15}$$

$$\begin{bmatrix} u_{M_i}^{M_i} \\ v_{M_i}^{M_i} \\ w_{M_i}^{M_i} \end{bmatrix} = \vec{T}_{BM_i} \begin{bmatrix} u_{M_i}^B \\ v_{M_i}^B \\ w_{M_i}^B \end{bmatrix} \tag{16}$$

Calculate local blade angle of attack from the local velocity in each blade coordinate system:

$$\alpha_{M_i} = \text{asin} \left[\frac{w_{M_i}^{M_i}}{\sqrt{u_{M_i}^{M_i^2} + w_{M_i}^{M_i^2}}} \right] \tag{17}$$

Determine lifting surface aerodynamic coefficients:

$$C_X^{M_i} = C_{X_0}^M(M) + C_{X\bar{\alpha}_{M_i}}^M(M) \sin \bar{\alpha}_{M_i} + C_{X\bar{\alpha}_{M_i}^2}^M(M) \sin^2 \bar{\alpha}_{M_i} \\ + C_{X\bar{\alpha}_{M_i}^3}^M(M) \sin^3 \bar{\alpha}_{M_i} + C_{X\bar{\alpha}_{M_i}^4}^M(M) \sin^4 \bar{\alpha}_{M_i} \quad (18)$$

$$C_l^{M_i} = C_{l_0}^M(M) + C_{l\bar{\alpha}_{M_i}}^M(M) \sin \bar{\alpha}_{M_i} + C_{l\bar{\alpha}_{M_i}^3}^M(M) \sin^3 \bar{\alpha}_{M_i} \quad (19)$$

$$C_N^{M_i} = C_{N_0}^M(M) + C_{N\alpha_{M_i}}^M(M) \sin \alpha_{M_i} + C_{N\alpha_{M_i}^3}^M(M) \sin^3 \alpha_{M_i} \\ + C_{N\alpha_{M_i}^5}^M(M) \sin^5 \alpha_{M_i} \quad (20)$$

$$C_m^{M_i} = C_{m_0}^M(M) + C_{m\alpha_{M_i}}^M(M) \sin \alpha_{M_i} + C_{m\alpha_{M_i}^5}^M(M) \sin^5 \alpha_{M_i} \quad (21)$$

The nonlinearity with angle of attack of the canard aerodynamics is captured by using appropriate data based on the magnitude of angle of attack. For example, the coupled solution can provide the canard aerodynamic data that may require one fit for low angles of attack and another for higher angles of attack.

Compute blade axial and normal forces and roll and pitching moments:

$$X_{M_i} = -Q_{M_i} S C_X^{M_i} \quad (22)$$

$$L_{M_i} = Q_{M_i} S D C_l^{M_i} \quad (23)$$

$$N_{M_i} = -Q_{M_i} S C_N^{M_i} \quad (24)$$

$$M_{M_i} = Q_{M_i} S D C_m^{M_i} - N_{M_i} (C G_N - C G_{N,A}) D \quad (25)$$

Transform these blade forces and moments in the blade coordinate system to the body-fixed coordinate system:

$$\begin{bmatrix} X_{M_i}^B \\ Y_{M_i}^B \\ Z_{M_i}^B \end{bmatrix} = \bar{T}_{BM_i}^T \begin{bmatrix} X_{M_i} \\ 0 \\ N_{M_i} \end{bmatrix} \quad (26)$$

$$\begin{bmatrix} L_{M_i}^B \\ M_{M_i}^B \\ N_{M_i}^B \end{bmatrix} = \bar{T}_{BM_i}^T \begin{bmatrix} L_{M_i} \\ M_{M_i} \\ 0 \end{bmatrix} \quad (27)$$

This aerodynamic model only serves as a framework since the amount, source, and type of aerodynamic data (experimental or computational, coefficients or forces/moments), as well as flight phenomena such as interactions, dependence on aerodynamic roll angle, etc., are specific to a particular airframe at a given stage in development. New aerodynamic models may be required every time the configuration is changed.

5. Model Geometry and Grid

The projectile modeled in this study has a length of 427 mm and a main diameter of 83 mm. The computational model, as shown in Fig. 2, has a hemispherical nose, 4 canards in front, and 10 fins at the back of the projectile. The main portion of the body consists of an 83-mm-diameter cylinder, which is followed by a conical boattail section. Two configurations, one with fins with a tab and the other with straight fins with no tabs, were modeled; however, the primary focus in this study has been the straight fins case.

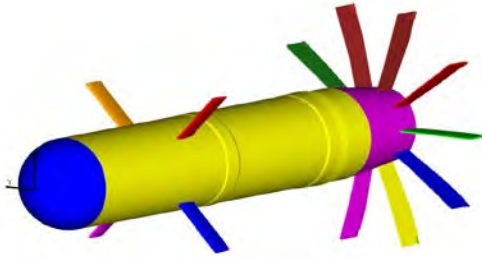


Fig. 2 Computational model of the projectile geometry

The computational grid for the main projectile body without the canards was created using MIME,²⁷ an unstructured mesh generator developed by Metacomp Technologies, Inc. GRIDGEN,²⁸ a commercially available software package, was used to generate structured meshes around the canards. The body alone computational mesh (Fig. 3) includes the body and the rear fins and consists of approximately 41 million cells. In general, most of the grid points were clustered in the boundary layer and the regions containing the nose canards and the afterbody fins. The boundary layer spacing normal to the wall was selected so that a wall function boundary condition could be used for turbulent flow. The first spacing near the wall was set at 0.25 mm on the body and 0.2 mm on the nose. A finer spacing of 3.5×10^{-3} mm was used on the fins and canards. These spacings resulted in y^+ values of 20 or less on most of the body and a little higher of the order of 30 on the nose. The y^+ values in the region containing the canards and the fins were 1.0 or less. The 4 nose canards were meshed separately and consisted of approximately 1.3 million cells each. These 4 canard meshes were then overset with the

background projectile body mesh using the Chimera procedure.²⁹ The final Chimera-overlapped mesh for each of the 2 (fin cant) models consists of approximately 43 million cells. A circumferential cross section (Fig. 4) shows full canard meshes. The outer boundaries of the canard meshes were chosen in a manner that required no cutting of the canard meshes by the main projectile body. However, the canards themselves were selected as cutters to cut holes in the background body mesh. A circumferential cut in the vicinity of the canards (Fig. 5) shows a cross-sectional view of the merged background and canard meshes after the cutting process was finished. The Chimera procedure requires proper transfer of information between the background mesh and the canard meshes at every time step. However, the advantage is that the individual grids are generated only once and the Chimera procedure can then be applied repeatedly as required during the canard motion. There is no need to generate new meshes at each time step during the canard control maneuvers for roll, pitch, and roll-pitch-yaw.

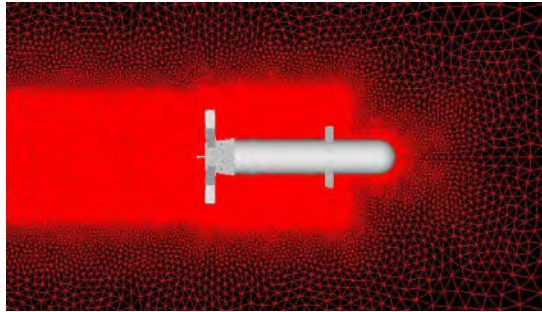


Fig. 3 Expanded view of the mesh in the XZ plane near the body

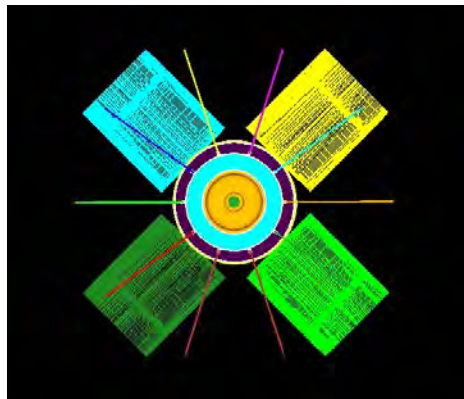


Fig. 4 View of the mesh in the circumferential plane, near the canard before oversight

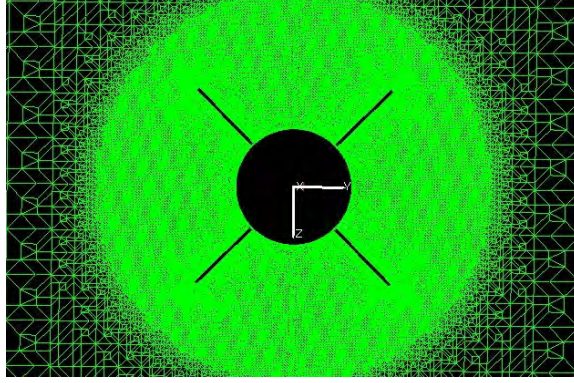


Fig. 5 View of the mesh in the circumferential plane, near the canards after overset cut

6. Results

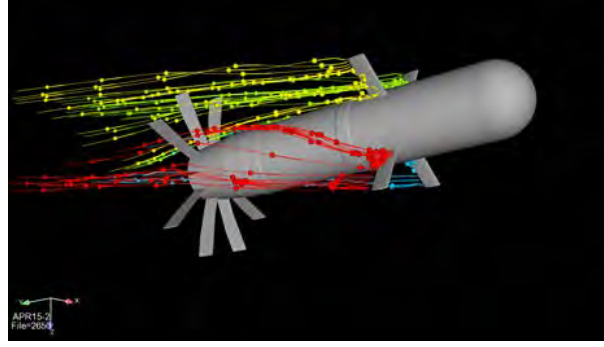
The constraints-based coupled CFD/RBD approach was used in time-accurate, coupled computations using Navier-Stokes techniques for a canard-controlled, finned projectile at $M = 0.6$. Both unsteady aerodynamics and flight dynamics were computed simultaneously and the flight response of the projectile was determined. In all cases, full 3-D solutions were obtained and no symmetry was used. The idea of the coupled approach was to capture static and dynamic aerodynamic behavior over short time durations (of the order of 0.5 s) with different motions. Three different motions, pure pitch, pure roll, and a roll-pitch-yaw motion, were considered in this study, and coupled calculations were performed for aerodynamic characterization that included complexities due to high angle of attack such as flow interactions and unsteadiness.

The analysis initially considers pure pitching and pure rolling motion before moving onto the coupled roll-pitch-yaw motion. This approach permits isolation of phenomena due to single DOF motion from full 3-D motion. Different DOF were enabled or disabled by setting the appropriate forces and/or moments in the 6DOF model to zero. In all cases, the Mach number is constant ($M = 0.6$). A time step of 0.0002 s was used in the time-accurate coupled calculations. Smaller time steps were also tested and computed results were found to change insignificantly. The results in this report focus on airframe motion from nonequilibrium points without control inputs (i.e., canard deflections). In some instances the virtual model is released from appreciable angle of attack (15°) to investigate phenomena such as flow separation. For the pure roll, the roll rate of the virtual model starts at 5 Hz and decreases with time. Table 1 shows the initial conditions for the different coupled simulation cases. Initial conditions include all 12 state variables. Cases 1, 2, and 3 represent the pure pitch, pure roll, and roll-pitch-yaw motion, respectively. Also, the canards are in the x orientation at the initial time ($t = 0$).

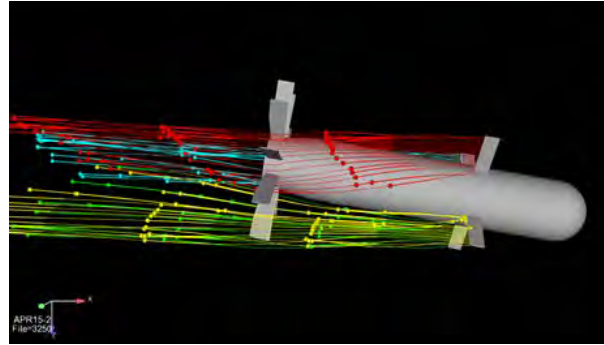
Table 1 Initial conditions for coupled simulations

	x (m)	y (m)	Z (m)	Φ (rad)	θ (rad)	Ψ (rad)	u (m/s)	v (m/s)	w (m/s)	P (rad/s)	q (rad/s)	r (rad/s)
Case1 (pitch)	0.0	0.0	0.0	0.0	0.2618	0.0	198.0	0.0	53.1	0.0	0.0	0.0
Case 2 (roll)	0.0	0.0	0.0	0.0	0.0	0.0	205.0	0.0	0.0	31.41593	0.0	0.0
Case 3 (roll- pitch- yaw)	0.0	0.0	0.0	0.0	0.2618	0.0	198.0	0.0	53.1	0.0	0.0	0.0

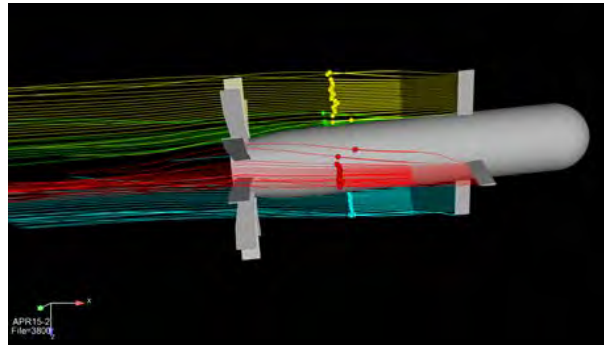
Some qualitative results are presented first for the roll-pitch-yaw motion (case 3). Figure 6 shows the particle traces emanating from the canards and moving downstream on the body and the fin region. The particle traces are shown at 3 different instants in time, $t = 0.03, 0.15$, and 0.26 s. As the projectile goes through the roll-pitch-yaw motion, the aerodynamic angles change with time and so does the interaction of the particle traces on the afterbody fins. The particle traces in Figs. 6a, 6b, and 6c are representative of a typical high positive angle of attack, high negative angle of attack, and almost zero degree angle of attack, respectively. Figure 7 shows vorticity contours at 6 different instants in time during the very initial phase of this roll-pitch-yaw motion, $0.02 \leq t \leq 0.07$ s. In this case, the projectile was released initially from an angle of attack of 15° . At time $t = 0.02$ s, the angle of attack is still close to 15° . As time increases, the angle of attack decreases and is close to almost zero degree angle of attack at $t = 0.07$ s. Near zero or small angles of attack ($t = 0.07$ s), the outboard or tip canard vortices can be clearly seen to propagate straight down, whereas the inboard or root canard vortices are weak and can barely be seen at $t = 0.07$ s. Specially, see the bottom canard facing the reader, the tip vortices move downstream and seem to hit one of the rear fins. As angle of attack is increased (time is decreased), the trajectory of the tip canard vortices changes, (i.e., it curves upwards over the length of the body, goes in between 2 rear fins at $t = 0.05$ s, and at high angles of attack of 15° , it hits the next rear fin [$t = 0.02$ s]). Also, it should be noted that root canard vortices, which are barely seen near zero degree angle of attack, can be seen at $t = 0.05$ s and very clearly at $t = 0.04$ s. At time, $t \leq 0.04$ s, root canard body vortices grows in strength and size and also seem to interact with the crossflow vortices at higher angles of attack. The resultant flow field is quite complex with flow interactions that affect the forces and moments and are automatically included in the coupled computations.



(a)



(b)



(c)

Fig. 6 Particle traces at 3 different instants in time during roll-pitch-yaw motion, $M = 0.6$, (a) $t = 0.03$, (b) $t = 0.15$, and (c) $t = 0.26$ s

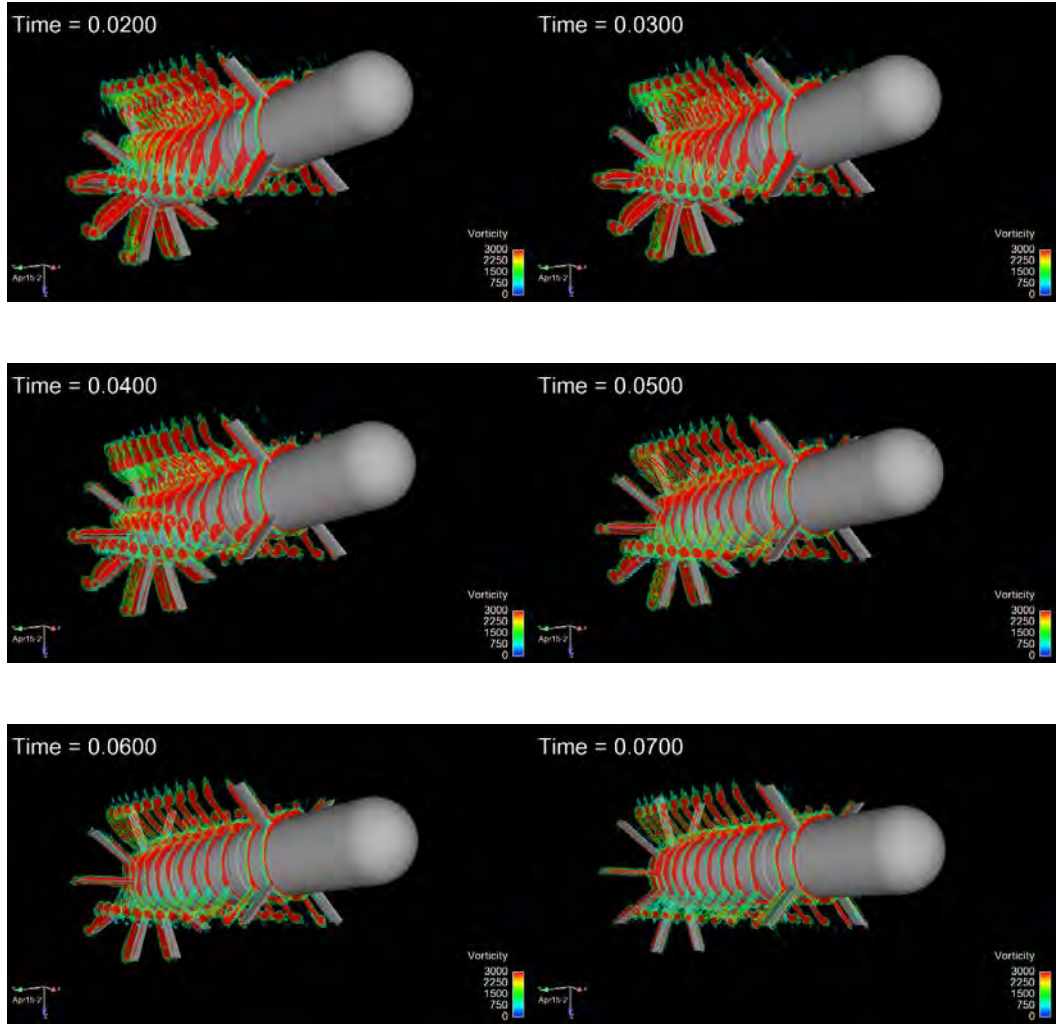


Fig. 7 Vorticity contours at different instants in time during initial phase of roll-pitch-yaw motion, $M = 0.6$, $0.02 \leq t \leq 0.07$ s

Figures 8 and 9 show the corresponding computed surface pressure contours at the same instants in time during the initial stage of the roll-pitch-yaw motion, $0.02 \leq t \leq 0.07$ s. Figure 8 shows the surface pressures on the full body; high pressures are shown in red and low pressures in blue. Near almost zero or small angles of attack ($t = 0.07$ s), the surface pressures are almost symmetric on the body other than the canards and fins, which can be clearly seen especially in the nose region. The surface pressure on each fin or canard is similar. Also, as expected, higher pressures in front of the nose, canards, and fins are evident. At earlier times, the angle of attack is as high as 15° ($t = 0.02$ s). With increasing angles of attack, the surface pressures become more and more asymmetric, with higher pressure on the wind-side and lower on the lee-side. Surface pressures on the body between the canards and the fins also get affected by canard root vortices. One can see this effect beginning at $t = 0.06$ s, which seems to get stronger at earlier times ($t = 0.05$ and 0.04 s) and more pronounced at higher angles of attack ($t = 0.03$ and 0.02 s). Similar effects can also be observed near the afterbody fin region (Fig. 9). This figure shows an expanded view of the surface pressures on the afterbody. It shows large asymmetric pressure distribution on the fins at early times largely due to higher angles of attack and canard-fin flow interactions. As angle of attack is decreased to almost zero ($t = 0.07$ s), these effects are no longer present and the pressures on each fin looks the same.

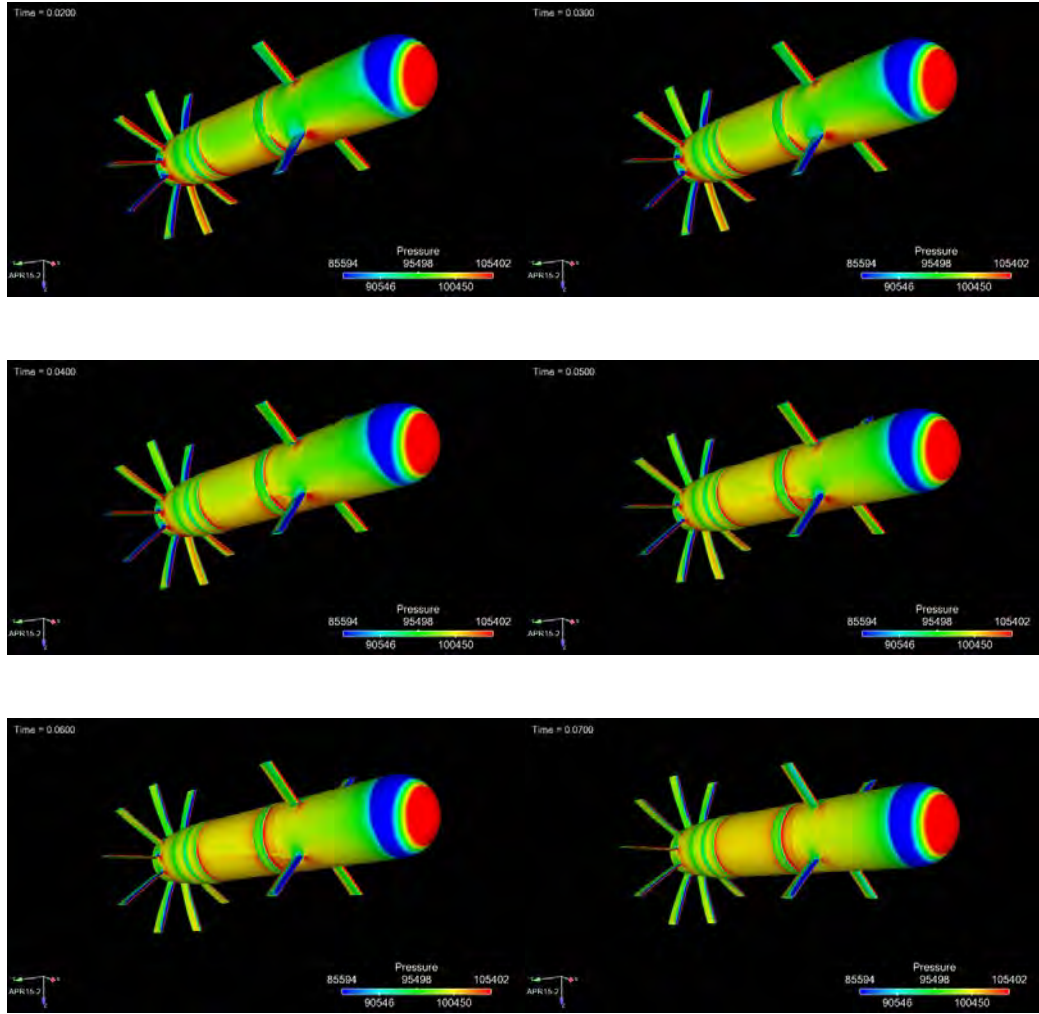


Fig. 8 Surface pressure contours at different instants in time during initial phase of roll-pitch-yaw motion, $M = 0.6$, $0.02 \leq t \leq 0.07$ s

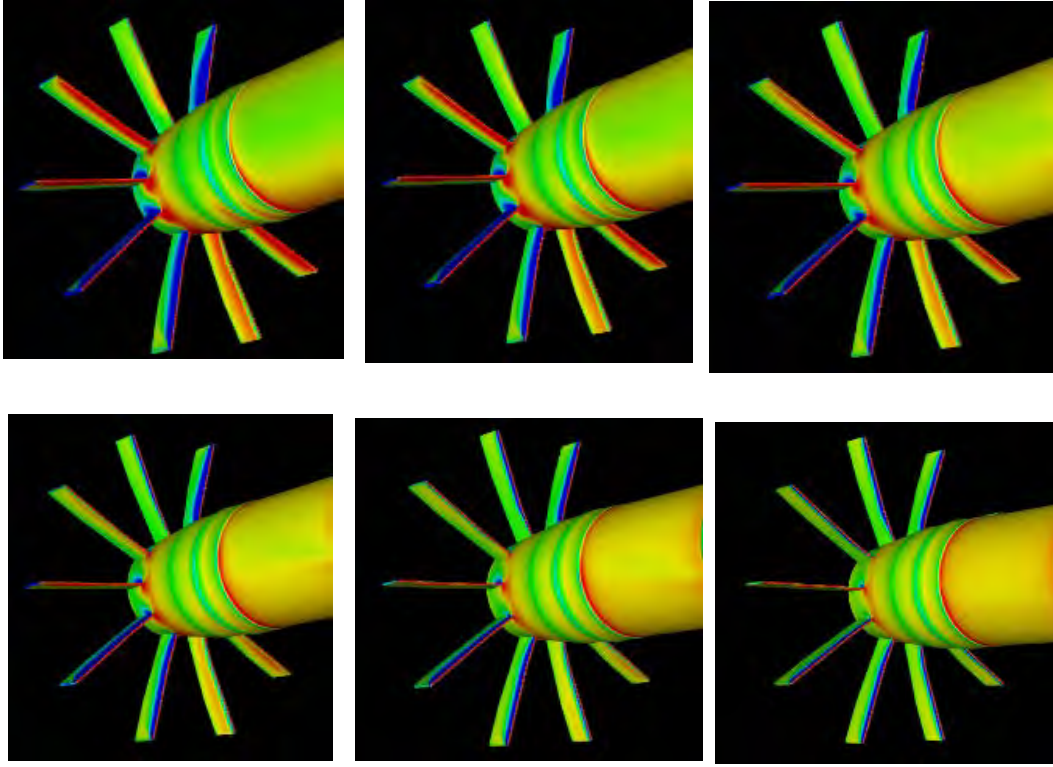


Fig. 9 Expanded view of surface pressure contours near the fins at different instants in time during initial phase of roll-pitch-yaw motion, $M = 0.6$, $0.02 \leq t \leq 0.07$ s

6.1 Pure Pitching Case

Figure 10 shows the pitching motion history for the pure pitching simulation. The body is released from 15° and damps to less than 2° within about 3.5 cycles of motion. For these constrained motion simulations, the Euler pitch angle and angle of attack are equivalent. The pitch rate starts at zero, is phase shifted by 90° from the pitch angle, and features some sharper peaks than the pitch angle.

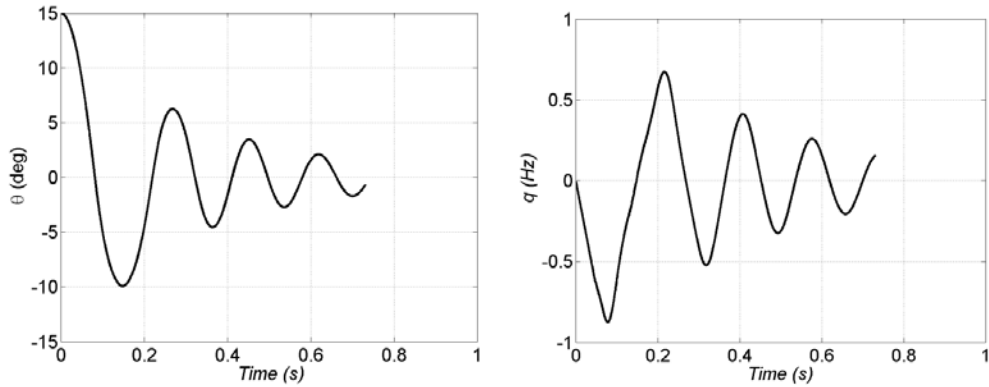


Fig. 10 Euler pitch angle (left) and pitch rate (right) for pure pitching case

The simulations compute the aerodynamic forces and moments acting on the body in addition to the angles and angular rates shown in Fig. 10. These data were analyzed to determine the aerodynamic coefficients at Mach 0.6. This technique, referred to as the direct method in this report, fit polynomials to the aerodynamic data as a function of angle of attack. Effects such as flow separation and vortex interactions were evident in most situations; therefore, the data were separated into low and high angle-of-attack regimes for analysis. Aerodynamic damping was appreciable in some instances (e.g., pitching moment). Damping contributions were removed to separate static and dynamic aerodynamics. The time history of the angular rates was used and the damping coefficient, based on reference diameter and velocity, was varied until hysteresis was removed in the curves of force or moment as a function of angle of attack. Semiempirical aeroprediction and virtual wind tunnel CFD techniques were used for the initial value of the damping coefficient. The final damping coefficient was then iteratively obtained when the total pitching moment (both static and dynamic components) matched computed total pitching moment.

Static aerodynamic forces and moments obtained from the direct method for the pure pitching simulation are provided in Figs. 11 and 12. In these figures, the data are presented with filled circles and the fits with lines. The low angle-of-attack data are given with blue circles and the high angle-of-attack data with green circles where applicable. The low angle-of-attack fits are a solid line and the high angle-of-attack fits are a dashed line.

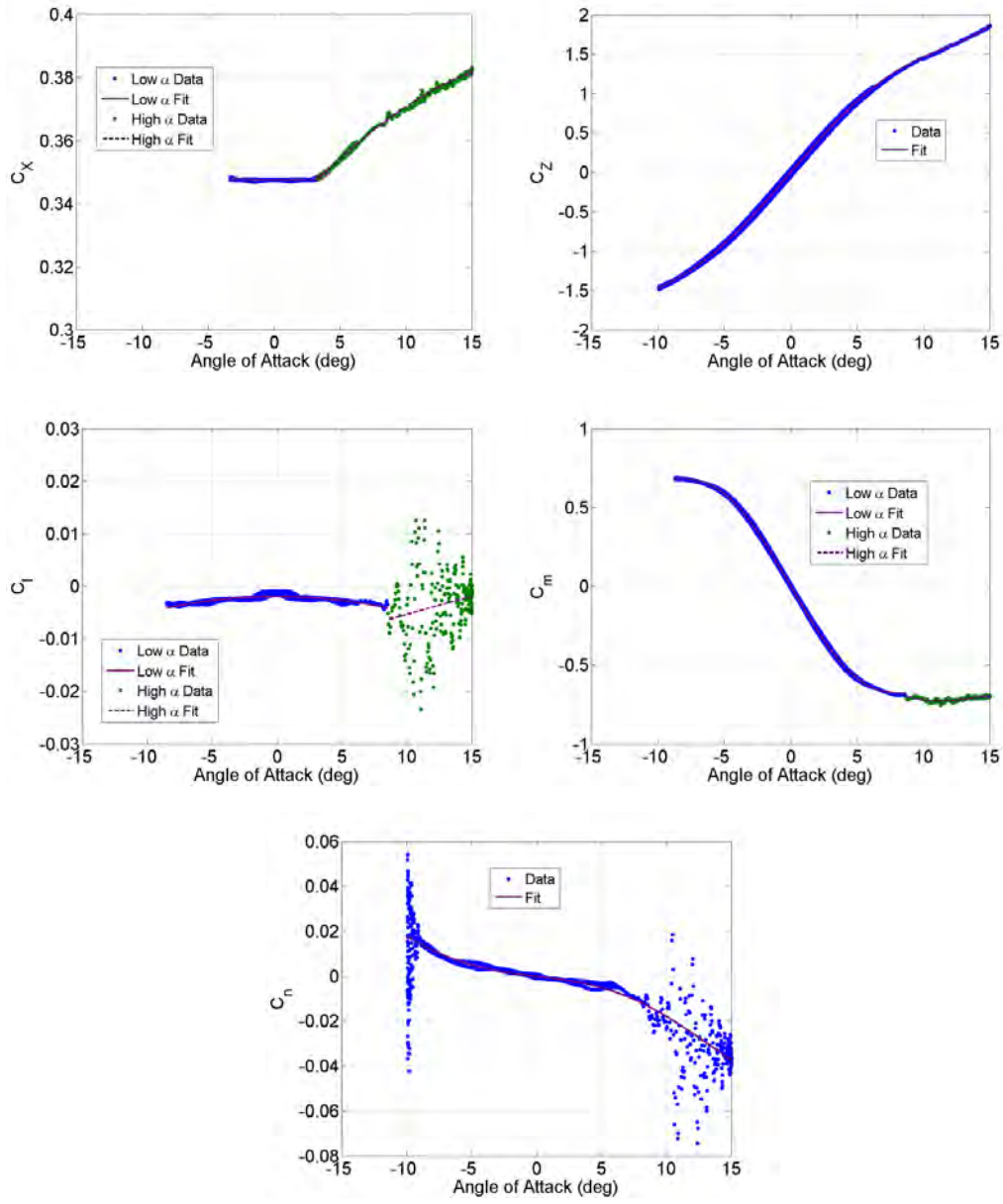


Fig. 11 Axial force coefficient of body-fin (top left), normal force coefficient of body-fin (top right), roll moment coefficient of body-fin (middle left), pitching moment coefficient of body-fin (middle right), and side moment of body-fin (bottom) from pure pitching motion

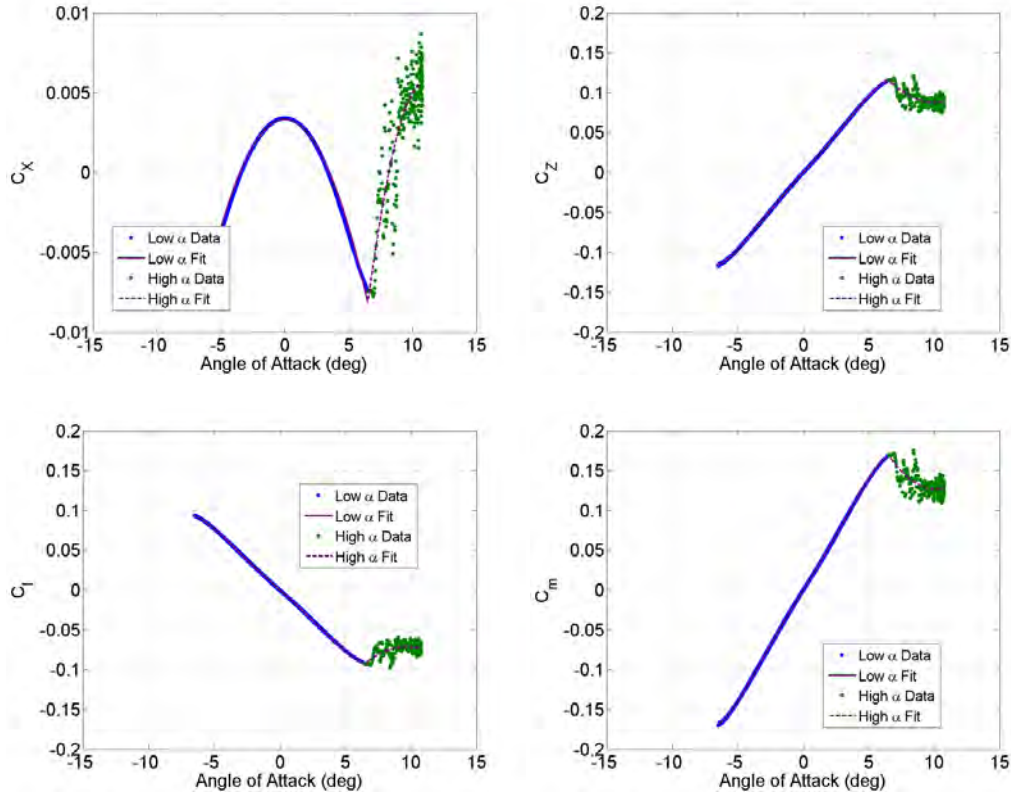


Fig. 12 Axial force coefficient of canard (top left), normal force coefficient of canard (top right), roll moment coefficient of canard (bottom left), and pitching moment coefficient of canard (bottom right) from pure pitching

The computations integrated pressure distributions over specific surfaces to obtain the aerodynamic forces and moments. The static aerodynamics for the body and fin surfaces (i.e., no canards) are shown in Fig. 11. The axial force coefficient is relatively flat for angles of attack below 33° . The high angle-of-attack data possess some fluctuation above 8° , potentially due to transient effects, and were fit with an odd-order polynomial. All normal force data were captured with a single odd-order polynomial. The normal force is nearly linear with the angle of attack until about 5° where the curve begins to fall off. The roll moment is small. In theory, the model does not possess roll inducing features (i.e., canted fins) so a nonzero roll moment indicates a truly 3-D flow or numerical asymmetries. At high angles of attack, there is a lot of scatter in the roll moment data suggesting unsteady phenomena. The pitching moment is strongly nonlinear with the angle of attack. The airframe is relatively less stable at higher angle of attack. Different odd-order polynomials were used for angles of attack below and above 8.7° . The fluctuation in the data for high angle of attack may again be attributed to transient effects. A small static side moment was evident in the data. A single curve was fit over all

angles of attack since this modeling approach cannot reproduce the large scatter for angles of attack higher than about 9° . It is difficult to determine exactly what produces the scatter in the data at high angle of attack for static side moment.

The aerodynamic forces and moments on an individual canard are presented in Fig. 12. The data collected in the coupled simulations were transformed from airframe body coordinates to a local canard body coordinate system for analysis (i.e., the angle-of-attack ranges are not the same between Figs. 12 and 11). The canard-alone axial force coefficient is much smaller than the contribution to total axial force from the body and fins. The canard axial force decreases with angle of attack until about 6.5° . At higher angle of attack, a different flow state is present that increases the axial force of the canard with angle of attack. The normal force, roll moment, and pitching moment of the canard increases almost linearly up to 6.5° angle of attack. Above 6.5° , stall reduces the effectiveness of the canards. A comparison of the fluctuating data with fits at high angle of attack highlights the difficulty in precisely modeling stall effects.

Tables 2 and 3 provide coefficients of the polynomial fits and relevant angle-of-attack ranges for the static aerodynamics of the body-fin and individual canard, which were discussed and shown in Figs. 11 and 12 for the pure pitching simulation.

Table 2 Aerodynamic coefficients for body-fin at Mach 0.6 from direct analysis of pure pitching

Order	C_x ($\alpha < 3.3^\circ$)	C_x ($\alpha \geq 3.3^\circ$)	C_N	C_i ($\alpha < 8.5^\circ$)	C_l ($\alpha \geq 8.5^\circ$)	C_m ($\alpha < 8.7^\circ$)	C_m ($\alpha \geq 8.7^\circ$)	C_n
0	0.347577	0.334976	0	-0.001956	-0.01235	0	-0.05491	0
1	0	0.228077	11.23991	0	0.040174	-8.3319	-5.83862	-0.0399
2	0.067352	0	0	-0.098564	0	0	0	0
3	0	-0.7185	-119.323	0	0	235.9846	79.66208	-2.529
5	0	0	879.0171	0	0	-2985.24	-442.231	15

Table 3 Aerodynamic coefficients for canard at Mach 0.6 from direct analysis of pure pitching

Order	C_x ($\alpha < 6.5^\circ$)	C_x ($\alpha \geq 6.5^\circ$)	C_N ($\alpha < 6.5^\circ$)	C_N ($\alpha \geq 6.5^\circ$)	C_l ($\alpha < 6.5^\circ$)	C_l ($\alpha \geq 6.5^\circ$)	C_m ($\alpha < 6.5^\circ$)	C_m ($\alpha \geq 6.5^\circ$)
0	0.003332	-0.06138	0	0.257626	0	-0.21496	0	0.38223
1	0	0.535632	1.048363	-1.45885	-0.8453	1.275679	1.529445	-2.18866
2	-0.90013	0	0	0	0	0	0	0
3	0	-5.08535	20.03176	15.87437	-13.7174	-14.8193	28.57757	23.76268
5	0	0	-1720.46	0	1200.296	0	-2455.96	0

In addition to the direct method, parameter estimation using a maximum likelihood method^{11,30–34} was conducted on the data for the pure pitching to obtain aerodynamic coefficients. This analysis assesses the aerodynamic model utility for use over a wider range of conditions and also permits more insight into the dynamic aerodynamic parameters. The aerodynamic coefficients from the direct method were used as the initial solution. The states measured from the CFD-RBD (black curves) and those calculated using the aerodynamic model (AM-RBD) in the parameter estimation (blue curves) are given in Fig. 13. The calculations faithfully follow the data; the root-sum-square fit error was 0.15° .

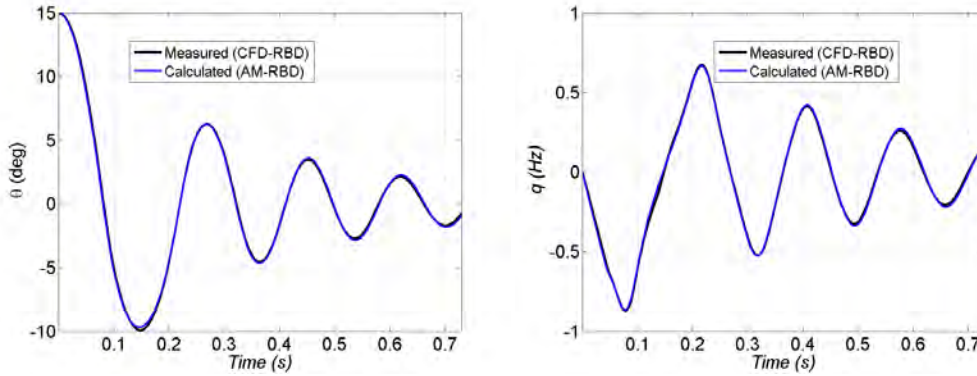


Fig. 13 States from parameter estimation analysis of pure pitching (Euler pitch angle root-sum-square fit error 0.15°)

Aerodynamic parameter estimation is often used in free-flight experiments, such as the spark range or onboard sensor technique, where flight motion (e.g., Euler angles, center-of-gravity position) is directly measured and the aerodynamic forces and moments required to produce that motion are inferred through analysis. In the CFD-RBD technique, the aerodynamic forces and moments are obtained in addition to the flight motions. This allows comparison of the measured and calculated aerodynamic forces and moments for different surfaces.

Moments that influence the pitching motion (e.g., pitching moment of body-fin, pitching moment of canards, and pitch damping moment of body-fin) are the only aerodynamic parameters that can be assessed using parameter estimation for the pure pitching. Figure 14 provides the time history of the pitching moment of the RAS (i.e., body-fin), MAS (i.e., canards), and total (i.e., body-fin and canards) for pure pitching. For about the first 0.05 s and a short timeframe near 0.15 s (as angle of attack remains above 8.7°), the pitching moment of the RAS is in the high angle-of-attack regime. Different parameters were adjusted in the estimation algorithm for the pitching moment of the RAS in the low and high angle-of-attack regimes. This process yielded the discontinuity in the calculated pitching moment for the

RAS near 0.05 s and underscores the challenge in modeling high angle-of-attack aerodynamics. A similar situation is encountered for the canard. The fluctuating data before 0.05 s and around 0.15 s indicates stall. The current analysis approach essentially fits through the fluctuation in the data, which changes the value of the higher-order terms in the aerodynamic model at or near the transition between low and high angle-of-attack coefficients. The correlation between unsteady fluctuations in the pitching moment of the body-fin and canards (e.g., before 0.05 s and around 0.15 s) and the fact that the canards are upstream of the body and fins suggest that fluctuations in the body-fin pitching moment are due to the interactions of stall-induced vortices shed off canards onto the body-fin pressure distribution. The body and finned surfaces could also be independently undergoing transient phenomena at these exact times/angles of attack but the visualizations do not support this claim. Further simulations could be conducted without canards to verify. The total pitching moment in Fig. 14 illustrates that this analysis captures appreciable nonlinearities, but the lack of agreement between measurements and calculations around 0.15 s highlights that more work remains in modeling high angle-of-attack aerodynamics (e.g., canard stall, vortex interactions).

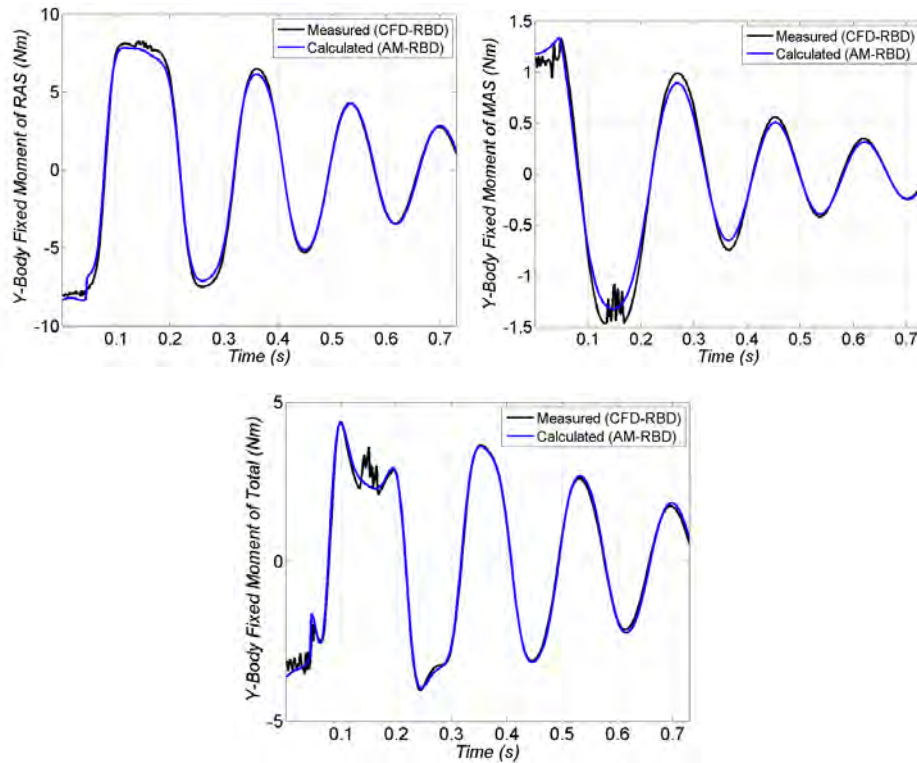


Fig. 14 Pitching moments from parameter estimation analysis for pure pitching (top left = body-fin, top right = individual canard, bottom = total)

Table 4 summarizes the aerodynamic coefficients obtained from parameter estimation for the pure pitching. This technique yielded a pitch damping moment of -80.7 for the body-fins. The pitch damping of the canards is implicitly contained in the flight model for the canards.

Table 4 Aerodynamic coefficients at Mach 0.6 from parameter estimation of pure pitching, $C_{m_q} = -80.7$

Order	Body-Fin		Canard	
	C_m	C_m	C_m	C_m
	$(\alpha < 10^\circ)$	$(\alpha \geq 10^\circ)$	$(\alpha < 7.05^\circ)$	$(\alpha \geq 7.05^\circ)$
0	0.0000	-0.3587	0.0000	0.1991
1	-8.033	-3.479	1.365	-0.269
3	240.28	49.22	14.96	0.00
5	-3505.5	-242.0	-990.7	0.0

6.2 Pure Rolling Case

The pure roll started with a 5-Hz roll rate. This allowed better characterization of the roll damping moment coefficient by increasing the relative contribution of roll damping to the dynamics. The measured and calculated roll angle and roll rate given in Fig. 15 agree well (root-sum-square fit error 0.1°). The roll rate decreases to near zero by 0.35 s and rotates about 155° in this time.

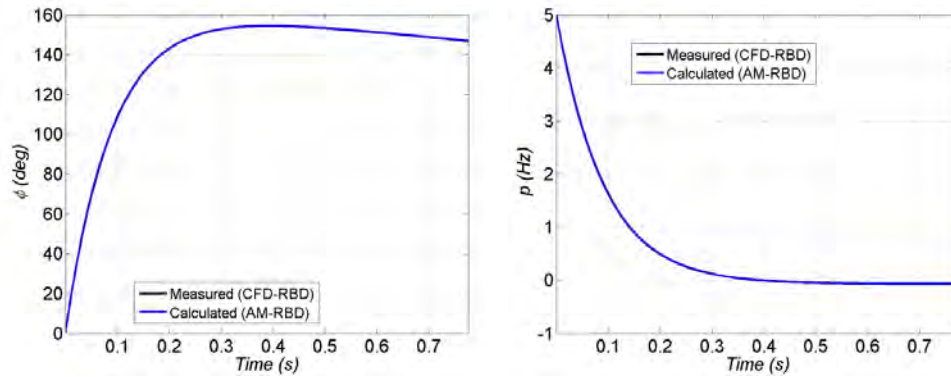


Fig. 15 States from parameter estimation analysis of pure rolling (Euler roll angle root-sum-square fit error 0.1°)

The roll moments are provided in Fig. 16 for the pure rolling motion. The largest roll moment is due to the roll damping of the RAS at higher roll rates. At later times when the roll rate is nearly zero, the small static roll moment is the main contributor to the RAS roll moment. The roll moment of the MAS is an order of magnitude smaller than the roll moment of the RAS over a majority of the time. There is some oscillation in the CFD-RBD data for times greater than about 0.4 s, but these values are very small.

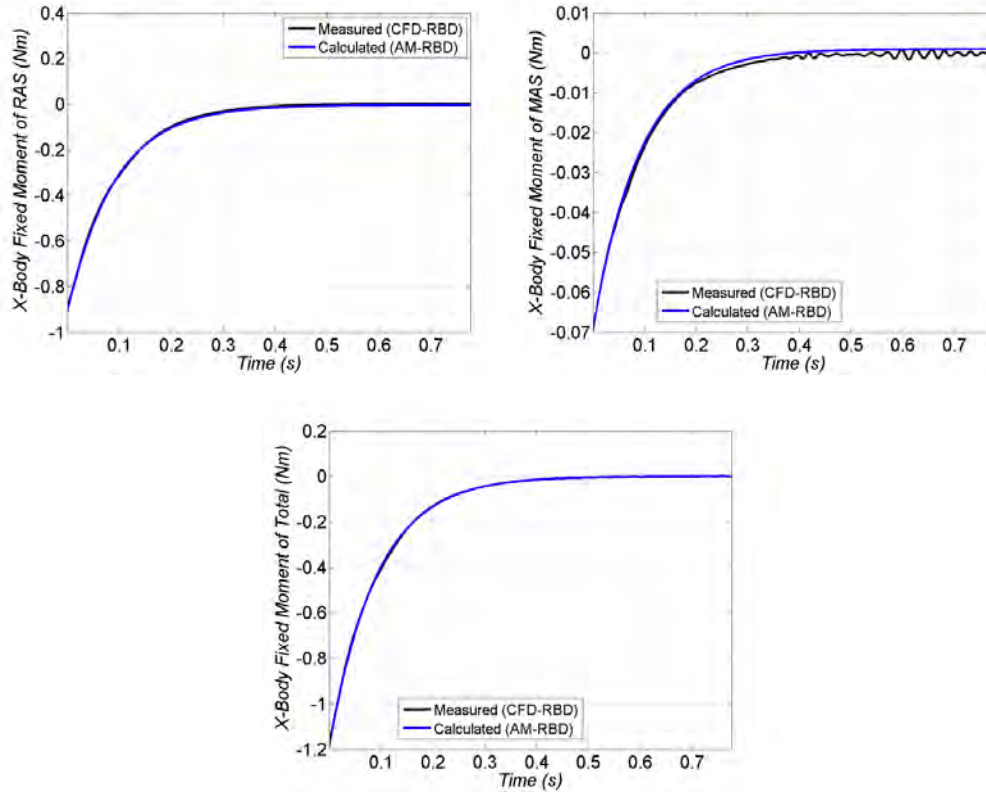


Fig. 16 Rolling moments from parameter estimation analysis for pure rolling (top left = body-fin, top right = individual canard, bottom = total)

The aerodynamic coefficients from parameter estimation for pure rolling are provided in Table 5. The roll damping moment coefficient for the body-fin was calculated as -12.1 .

Table 5 Aerodynamic coefficients at Mach 0.6 from parameter estimation of pure rolling, $C_{l_p} = -12.1$

Order	Body-Fin C_l	Canard C_l
0	-0.00078	0
1	0	-0.695
3	0	-15.68
5	0	1251.2

6.3 Roll-Pitch-Yaw Case

Analysis of pure pitch and pure roll isolated the flight behaviors in those DOF. The roll-pitch-yaw case seeks to identify how coupling these DOF in a more realistic sense changes the flight response. The direct method was applied to the roll-pitch-yaw flight data to determine static aerodynamic coefficients. These results are shown in Figs. 17 (body-fin) and 18 (canard). Direct method results for the pure pitching and the coupled roll-pitch-yaw are virtually identical. The only significant difference is for the aerodynamics of the canard at high angle of attack. The pure pitching predicts a slightly decreasing response in the coefficients poststall and the roll-pitch-yaw increases slightly with angle of attack.

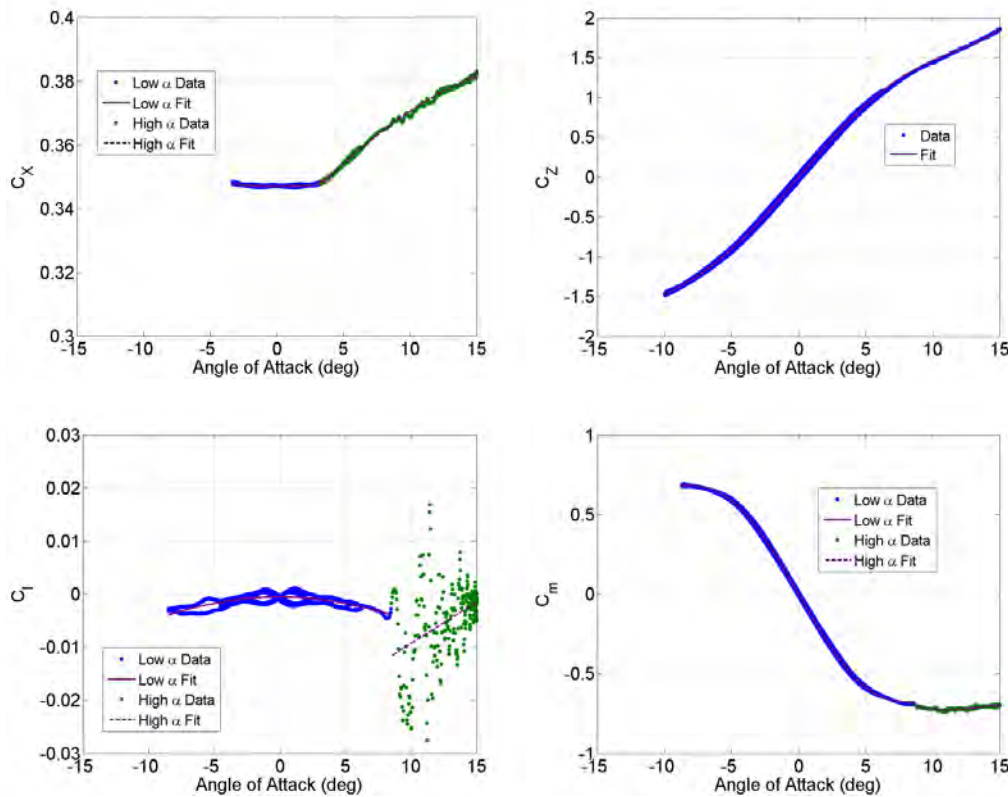


Fig. 17 Axial force coefficient of body-fin (top left), normal force coefficient of body-fin (top right), roll moment coefficient of body-fin (bottom left), and pitching moment coefficient of body-fin (bottom right) from roll-pitch-yaw motion

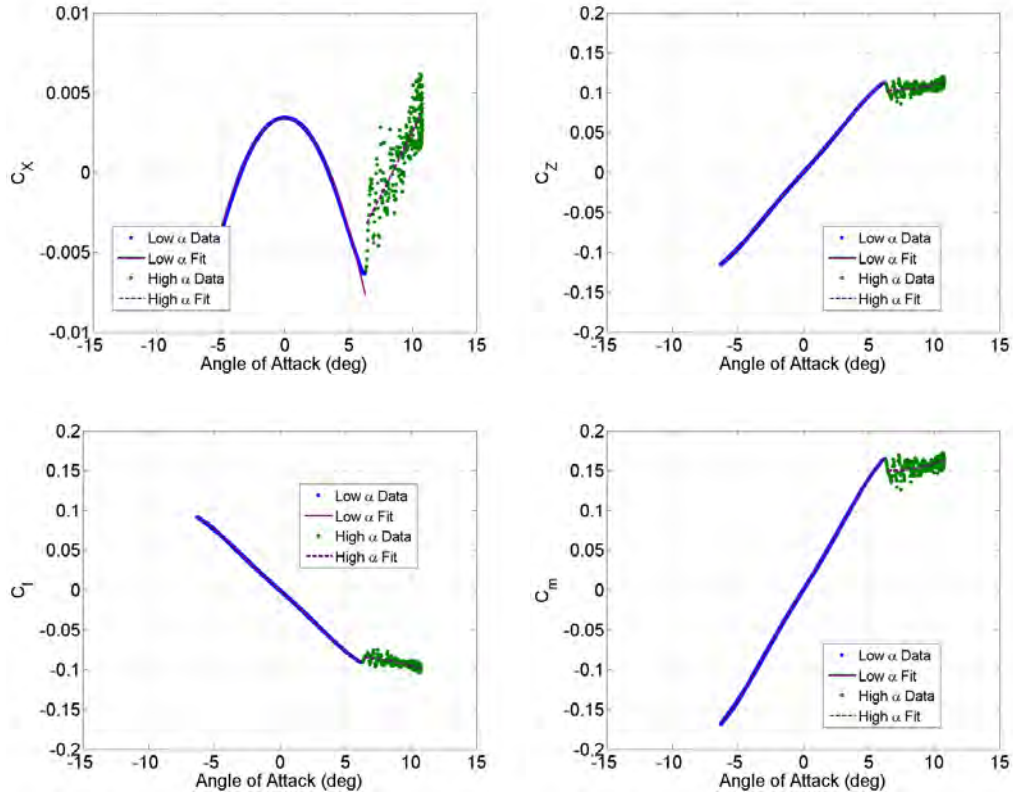


Fig. 18 Axial force coefficient of canard (top left), normal force coefficient of canard (top right), roll moment coefficient of canard (bottom left), and pitching moment coefficient of canard (bottom right) from roll-pitch-yaw motion

The parameter estimation results for the roll-pitch-yaw are discussed next. Figure 19 shows favorable agreement between the measured and calculated roll, pitch, and yaw Euler angles. The root-sum-square fit errors were 0.32° for roll, 0.19° for pitch, and 0.11° for yaw. Similar to the pure pitch, the airframe was initially pitched up to 15° and damps to about 2° within 4 cycles of motion. The small static roll moment, however, causes this 3DOF case to roll over 30° (counterclockwise when viewed from behind airframe) in this time. As the body rolls, the yaw Euler angle increases. Additional motion out of the pitch plane is produced by the small static side moment.

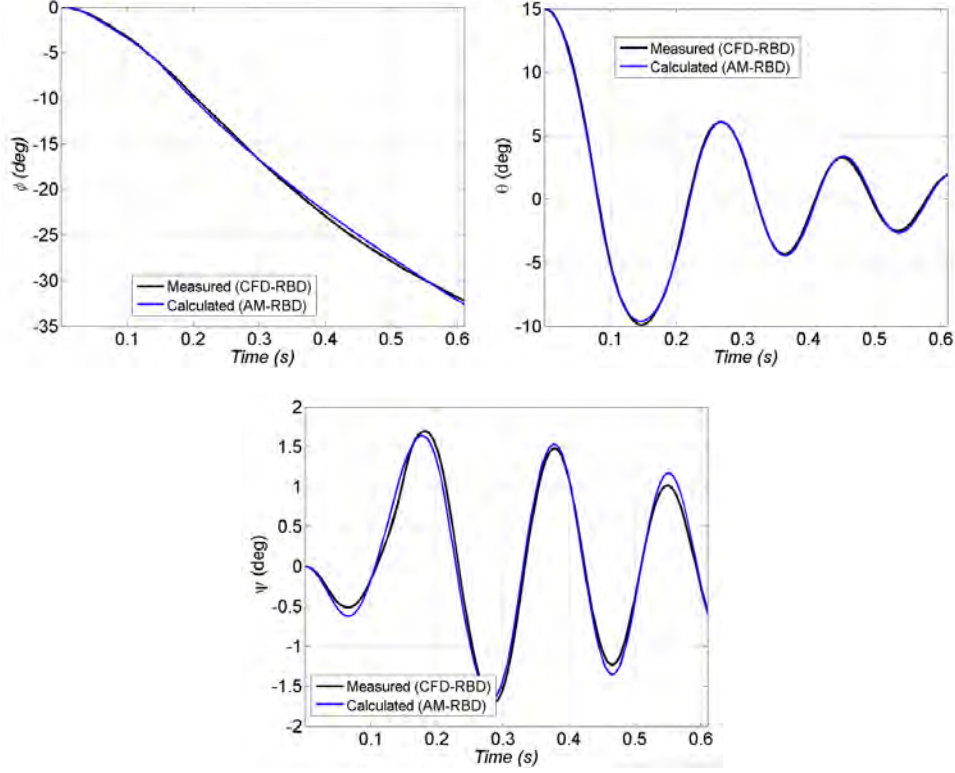


Fig. 19 Euler roll (top left), pitch (top right), and yaw (bottom) angles from parameter estimation analysis of roll-pitch-yaw (root-sum-square fit errors of 0.32° , 0.19° , and 0.19° in Euler roll, pitch, and yaw angles)

Measured and calculated roll, pitch, and yaw body rates are given in Fig. 20. Similar to the pure pitching case, there is excellent agreement between the measured (coupled solution) pitch rate and the computed (or modeled) pitch rate. Note that the pitch rate is an order of magnitude higher than the roll and yaw rate. In general, the roll rate and the yaw rate also match reasonably well between the measurements and calculations as expected because the angles agree as favorably as shown in Fig. 19. There are some finely detailed, complex behaviors (e.g., roll rate) that the parameter estimation appears to capture. There are some discrepancies that can be observed near $t = 0.15$ s and are attributable to unsteady flow interaction effects.

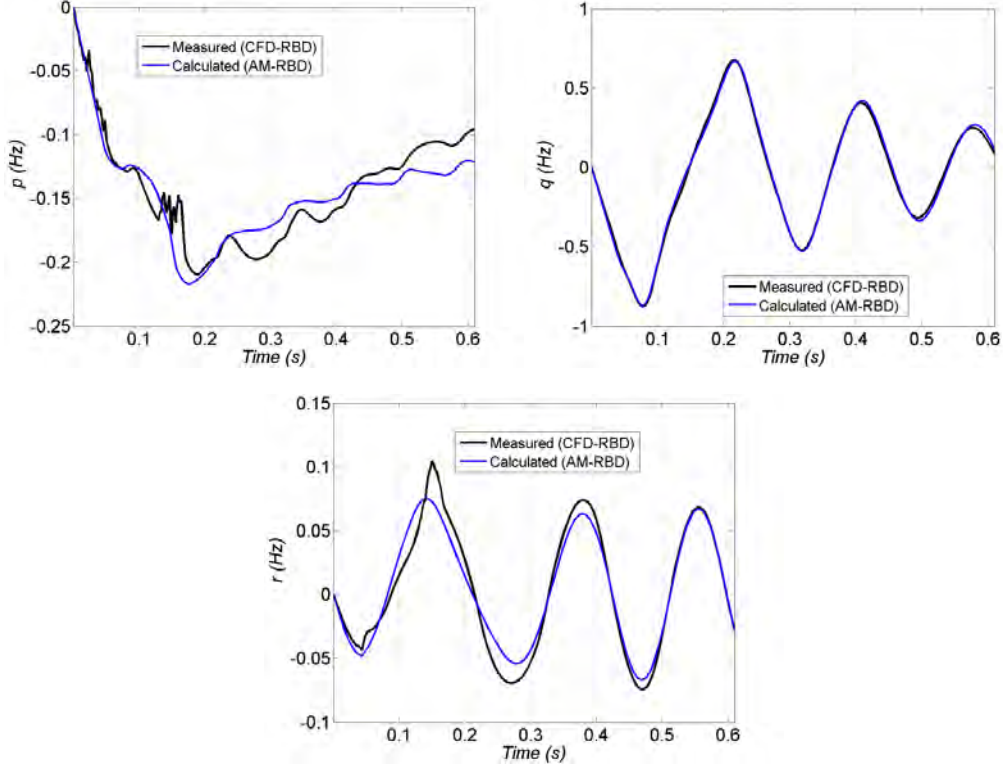


Fig. 20 Roll (top left), pitch (top right), and yaw (bottom) rates from parameter estimation analysis of roll-pitch-yaw

The total (body-fin and canard) aerodynamic moments that yield the kinematics and dynamics shown in Figs. 19 and 20 are provided in Fig. 21. Again, roll and yaw moments are an order of magnitude lower than pitch moments. The pitch moment illustrates a high degree of nonlinearity as discussed for the pure pitching case. The fluctuation in the pitch moment prior to 0.05 s and around 0.15 s again suggests unsteadiness due to canard stall. This fluctuation is also apparent in the roll and yaw moments at these times. A canard-on-body-fin flow interaction is offered to explain fluctuation in body-fin aerodynamics (not shown for roll-pitch-yaw) during periods of canard stall and is also supported by the flow visualization, but this hypothesis needs to be tested with further analysis. Capturing these high angle-of-attack phenomena is critical to understanding the flight behaviors since these fluctuations in the aerodynamic moments propagate through the dynamics and emerge as the sharp nonlinearities, for example, as seen in the roll rate and yaw rate around 0.15 s in Fig. 20.

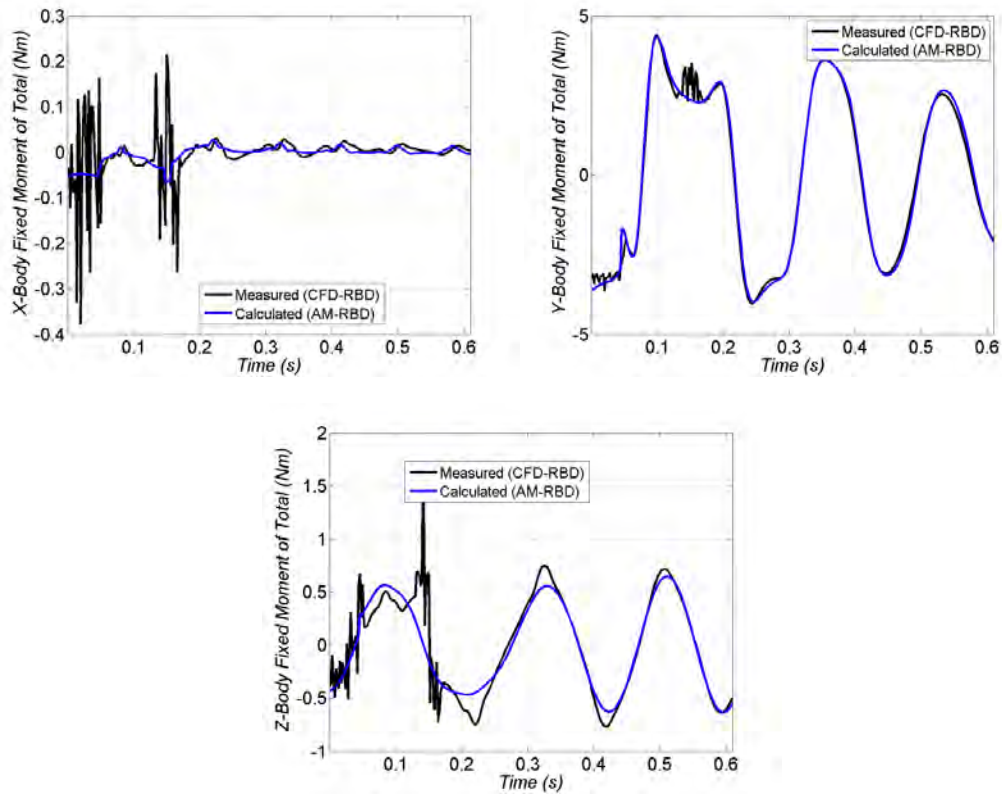


Fig. 21 Total moments from parameter estimation analysis for roll-pitch-yaw (top left = roll, top right = pitch, bottom = yaw)

Figure 22 compares the aerodynamic moments obtained from the direct method and parameter estimation (numerical values provided in the Appendix). The 2 methods reasonably agree. Some discrepancies can be observed, for example, in canard roll moment and especially at higher angles of attack. Models underpinning both datasets clearly need to be refined to better account for unsteady high angle-of-attack aerodynamics. Overall, the data provided by the pure pitch and pure roll analysis yield a reasonable prediction of the coupled roll-pitch-yaw behavior. This is supported by the agreement between the results in Fig. 22 for the parameter estimation and direct method (i.e., input to parameter estimation routine). Capturing the rapidly fluctuating aerodynamic forces and moments on the afterbody-fins due to vortex interactions during time periods of canard stall appears to be the prime motivator for performing roll-pitch-yaw simulations.

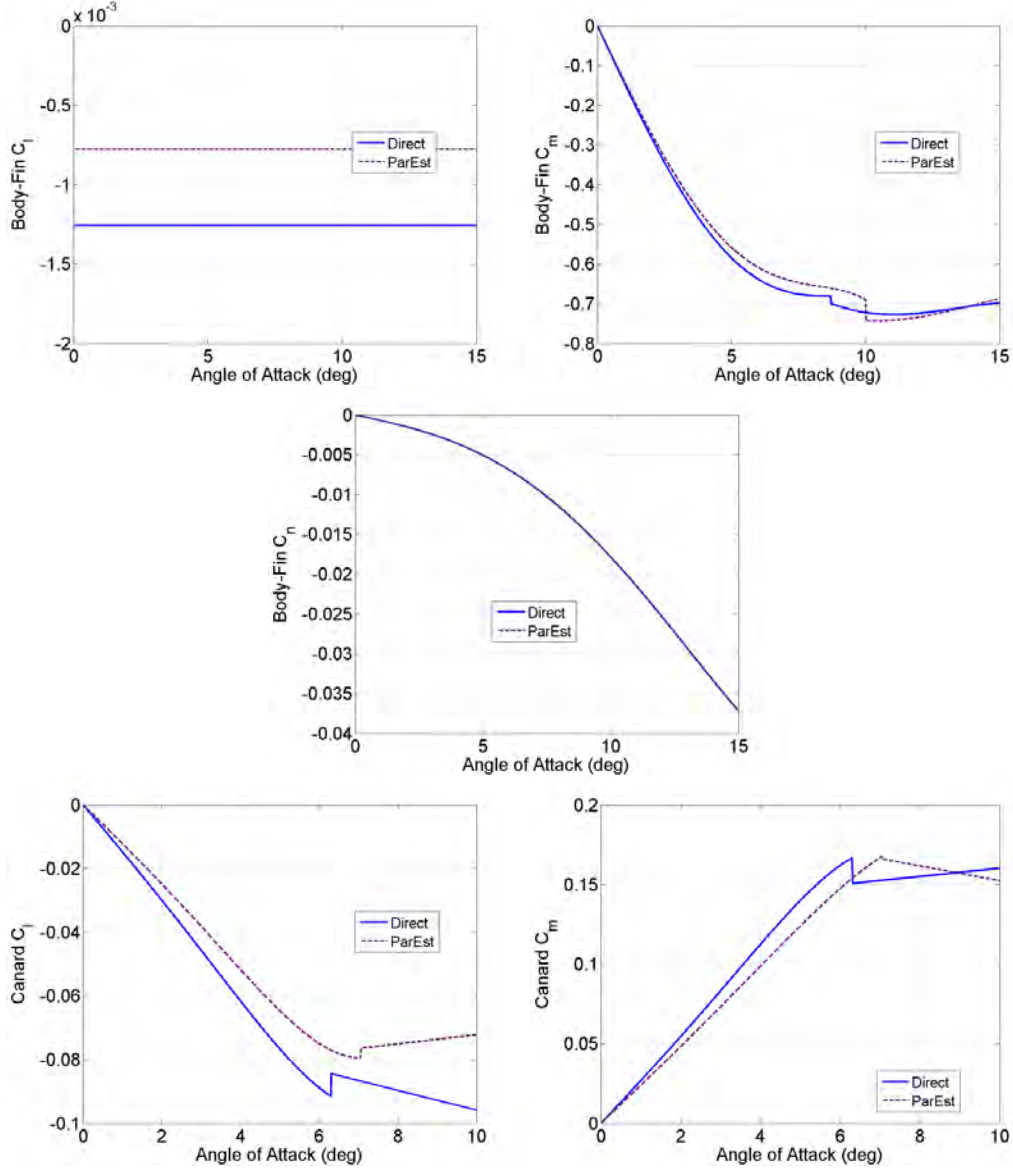


Fig. 22 Rolling moment coefficient of body-fin (top left), pitching moment coefficient of body-fin (top right), side moment coefficient of body-fin (middle), rolling moment coefficient of canard (bottom left), and pitching moment coefficient of canard (bottom right) from direct method and parameter estimation of roll-pitch-yaw

7. Conclusions

New constraints-based computations were performed on a canard-controlled finned projectile using a coupled CFD/RBD procedure and a 3-D, unsteady, unstructured Navier-Stokes technique. In the coupled calculations, both unsteady aerodynamics and flight dynamics were computed simultaneously and the response of the projectile was determined in pure pitch, pure roll, and roll-pitch-yaw motions. A full aerodynamic model, including separate body-fin and canard contributions for

this configuration, was generated from the coupled solutions using parameter estimation algorithms and a direct method. Comparison of the coupled solutions and the aerodynamic model shows generally good agreement indicating that the aerodynamic model sufficiently characterizes flight motions for this configuration with the exception of high angle of attack. Computed flow fields show unsteady vortices during canard stall that yield canard-on-afterbody-fin flow interactions at high angles of attack resulting in unsteady aerodynamic forces/moments. It is important to note that these unsteady effects are automatically taken into account in the coupled approach. Aerodynamic models for this situation, potentially including the stochastic nature of the aerodynamic forces and moments during high angle of attack, need to be improved. In addition, these results suggest that isolating the pitch and roll dynamics and using this analysis to predict the coupled roll-pitch-yaw motion is appropriate for low angle of attack. At higher angle of attack, the unsteadiness and interactions may require more sophisticated analysis techniques.

This approach based on new constraints-based coupled fly-out simulations to generate aerodynamics for pitch, roll, and pitch-roll-yaw flights shows good promise. The same constrained-based coupled fly-out simulation approach can be easily extended for aerodynamic/flight dynamic characterization with canard deflections. For guided flights with deflecting canards, control algorithms need to be developed and implemented in coupled CFD/RBD simulations. Ongoing efforts are focused on coupled calculations for pitch, roll, and roll-pitch-yaw control maneuvers with canard deflections, both open-loop and closed-loop. These results will illustrate the utility of high fidelity modeling of the flight physics in the control formulation.

8. References

1. PRODAS user manual. South Burlington (VT): Arrow Tech Assoc; 1997.
2. Moore FG, Moore LY. Approximate method to calculate nonlinear rolling moment due to differential fin deflection. *Journal of Spacecraft and Rockets*. 2012;49(2):250–260.
3. Fresconi FE, DeSpirito JS, Celmins I. Flight performance of a small diameter munition with a rotating wing actuator. *Journal of Spacecraft and Rockets*. Vol. 2015;42(2):305–319.
4. Fresconi FE, Celmins I, Ilg M, Maley J. Projectile roll dynamics and control with a low-cost skid-to-turn maneuver system. *Journal of Spacecraft and Rockets*. 2014;51(2):624–627.
5. Dupuis A, Hathaway W. Aeroballistic range tests of the basic finner reference projectile at supersonic velocities. Valcartier (Canada): Defence Research Establishment Valcartier; 1997 Aug. Report No.: DREV-TM-9703.
6. Fresconi FE, Guidos B, Celmins I, Hathaway W. Flight behavior of an asymmetric body through spark range experiments using roll-yaw resonance for yaw enhancement. Aberdeen Proving Ground (MD): Army Research Laboratory (US); 2015. Report No.: ARL-TR-7334. Also available at: http://www.arl.army.mil/www/default.cfm?technical_report=7420.
7. Fresconi FE, Harkins T. Experimental flight characterization of asymmetric and maneuvering projectiles from elevated gun firings. *Journal of Spacecraft and Rockets*. 2012;49(6):1120–1130.
8. Sahu J. Numerical computations of dynamic derivatives of a finned projectile using a time-accurate CFD Method. Reston (VA): American Institute of Aeronautics and Astronauts; 2007 Aug. AIAA Paper 2007-6581.
9. Siltan S. Navier-Stokes computations for a spinning projectile from subsonic to supersonic speeds. *Journal of Spacecraft and Rockets*. 2005;42(2):223–231.
10. DeSpirito J. Lateral jet interaction on a finned projectile in supersonic flow. 50th AIAA Aerospace Sciences Meeting including the New Horizons Forum and Aerospace Exposition 2012. 2012 Jan 9–12; Nashville, TN. Red Hook (NY): Curran Associates, Inc.; 2012 Oct. Vol. 1, p. 5953.

11. Ericsson LE, Reding JP. Steady and unsteady vortex-induced asymmetric loads on slender vehicles. *Journal of Spacecraft and Rockets*. 1981;18(2):97–109.
12. Sahu J, Fresconi FE. Aeromechanics and control of projectile roll using coupled simulation techniques. *Journal of Spacecraft and Rockets*. 2015;52(3):954–957.
13. Sahu J, Heavey KR. Time-accurate computations for rapid generation of missile aerodynamics. *AIAA Atmospheric Flight Mechanics Conference* 2010. 2010 Aug 2–6; Toronto, Canada. Red Hook (NY): Curran Associates, Inc.; 2011 Mar. Vol. 3, p. 2016.
14. Sahu J, Heavey KR. Unsteady CFD modeling of micro-adaptive flow control for an axisymmetric body. *International Journal of Computational Fluid Dynamics*. 2006;20(5):271–278.
15. Sahu J. Time-accurate numerical prediction of free-flight aerodynamics of a finned projectile. *AIAA Journal of Spacecraft and Rockets*. 2008;45(5):946–954.
16. Sahu J. Unsteady free flight aerodynamics of a spinning projectile at a high transonic speed. *AIAA Atmospheric Flight Mechanics Conference* 2008. 2008 Aug 18–22; Honolulu, HI. Red Hook (NY): Curran Associates, Inc.; 2009 Apr. Vol. 3, p. 1602.
17. Costello M, Sahu J. Using computational fluid dynamic/rigid body dynamic results to generate aerodynamic models for projectile flight simulation. *Journal of Aerospace Engineering*. 2008;22(G7):1067–079.
18. Sahu J. Computations of unsteady aerodynamics of a spinning body at transonic speeds. *27th AIAA Applied Aerodynamics Conference* 2009. 2009 Jun 22–25; San Antonio, TX. Red Hook (NY): Curran Associates, Inc.; 2009 Aug. Vol. 1, p. 649.
19. Sahu J. Virtual fly-out simulations of a spinning projectile from subsonic to supersonic speeds. *29th AIAA Applied Aerodynamics Conference* 2011. 2011 Jun 27–30; Honolulu, HI. Red Hook (NY): Curran Associates, Inc.; 2011 Nov. Vol. 1, p. 414.
20. Sahu J. Time-accurate computations of free-flight aerodynamics of a spinning projectile with and without flow control. Aberdeen Proving Ground (MD): Army Research Laboratory (US); 2006 Sep. Report No.: ARL-TR-3919. Also available at http://www.arl.army.mil/www/default.cfm?technical_report=1251.

21. Sahu J, Fresconi F, Heavey K. Unsteady aerodynamics of a finned projectile at a supersonic speed with jet interaction. 32nd AIAA Applied Aerodynamics Conference 2014 held at the AIAA Aviation Forum 2014; 2014 Jun 16–20; Atlanta, GA. Red Hook (NY): Curran Associates, Inc.; 2014 Sep. Paper 2014-3024; Vol. 5, p. 3333.
22. Sahu J. Unsteady aerodynamic simulations of a canard-controlled projectile at low transonic speeds. AIAA Atmospheric Flight Mechanics Conference 2011; 2011 Aug 8–11; Portland, OR. Red Hook (NY): Curran Associates, Inc.; 2012 Feb. Vol. 1, p. 532.
23. Sahu J, Costello M, Montalvo C. Development and application of multidisciplinary computational techniques for projectile aerodynamics. 7th International Conference on Computational Fluid Dynamics (ICCFD7); 2012 Jul 9–13; Big Island, HI. Paper No. ICCFD7-4504.
24. Peroomian O, Chakravarthy S, Goldberg U. A ‘grid-transparent’ methodology for CFD. Reston (VA): American Institute of Aeronautics and Astronauts; 1997. AIAA Paper 97-07245.
25. Peroomian O, Chakravarthy S, Palaniswamy S, Goldberg U. Convergence acceleration for unified-grid formulation using preconditioned implicit relaxation. 36th AIAA Aerospace Sciences Meeting and Exhibit; 1998 Jan 12–15; Reno, NV. AIAA Paper 98-0116; 1998.
26. Goldberg UC, Peroomian O, Chakravarthy S. A wall-distance-free k-e model with enhanced near-wall treatment. ASME Journal of Fluids Engineering. 1998;120:457–462.
27. MIME user’s manual. Agoura Hills (CA): Metacomp Technologies; 2012.
28. Gridgen version 15 user’s manual. Bedford (TX): Pointwise, Inc.; 2005.
29. Steger J, Dougherty C, Benek J. A Chimera grid scheme. Advances in grid generation. Fairfield (NJ): American Society of Mechanical Engineers; 1983. ASME FED-Vol. 5.
30. Chapman G, Kirk D. A new method for extracting aerodynamic coefficients from free-flight data. AIAA Journal. 1970;8(4):753–758.
31. Whyte RH, Mermagen WH. A method for obtaining aerodynamic coefficients from Yawsonde and radar data. Journal of Spacecraft and Rockets. 1973;10(6):384–388.

32. Hathaway W, Whyte R. Aeroballistic research facility free flight data analysis using the maximum likelihood method. Eglin Air Force Base (FL): Air Force Armament Laboratory (US); 1979 Dec. Report No.: AFATL-TR-79-98.
33. Iliff K. Parameter estimation for flight vehicles. *Journal of Guidance*. 1989;12(5):609–622.
34. Klein V, Morelli EA. Aircraft system identification. AIAA Education Series. Reston (VA): American Institute of Aeronautics and Astronauts; 2006.

Appendix. Aerodynamic Coefficients at Mach 0.6

Table A-1 Aerodynamic coefficients at Mach 0.6 from direct and parameter estimation analysis of roll-pitch-yaw

O r d e r	Body-Fin C_l		Canard C_l (low α)		Canard C_l (high α)		Body-Fin C_n	
	Direct	Parameter Estimation	Direct ($\alpha < 6.3^\circ$)	Parameter Estimation ($\alpha < 7.05^\circ$)	Direct ($\alpha \geq 6.3^\circ$)	Parameter Estimation ($\alpha \geq 7.05^\circ$)	Direct	Parameter Estimation
0	-0.00126	-0.00078	0	0	-0.064654	-0.0867	0	0
1	0	0	-0.84469	-0.695	-0.179914	0.083591	-0.03991	-0.03991
3	0	0	-13.9344	-15.68	0	0	-2.52907	-2.52907
5	0	0	1229.269	1251.2	0	0	14.61258	14.61258

O r d e r	Body-Fin C_m (low α)		Body-Fin C_m (high α)		Canard C_m (low α)		Canard C_m (high α)	
	Direct ($\alpha < 8.7^\circ$)	Parameter Estimation ($\alpha < 10^\circ$)	Direct ($\alpha \geq 8.7^\circ$)	Parameter Estimation ($\alpha \geq 10^\circ$)	Direct ($\alpha < 6.3^\circ$)	Parameter Estimation ($\alpha < 7.05^\circ$)	Direct ($\alpha \geq 6.3^\circ$)	Parameter Estimation ($\alpha \geq 7.05^\circ$)
0	0	0	-0.08071	-0.3587	0	0	0.134338	0.1991
1	-8.33163	-8.033	-5.64646	-3.479	1.52846	1.365	0.148636	-0.269
3	236.0836	240.28	77.98839	49.22	28.79212	14.96	14.41674	0
5	-2997.08	-3505.5	-438.128	-242	-2465.12	-990.7	0	0

List of Symbols, Abbreviations, Acronyms, and Nomenclature

3-D	3-dimensional
CFD	computational fluid dynamics
DOF	degrees of freedom
MAS	moveable aerodynamic surfaces
RAS	rigid aerodynamic surfaces
RBD	rigid body dynamics
ϕ, θ, ψ	Euler roll, pitch, and yaw angles, rad
I	moment-of-inertia tensor, kg m ²
m	mass, kg
D	diameter, m
$S = \frac{\pi}{4} D^2$	reference area, m ²
V	velocity, m/s
M	Mach number
$\alpha, \beta, \bar{\alpha}, \phi_A$	pitch angle of attack, yaw angle of attack, total angle of attack, aerodynamic roll angle, rad
ρ	atmospheric density, kg/m ³
$\bar{q} = \frac{1}{2} \rho V^2$	dynamic pressure, Pa
x_B, y_B, z_B	body-fixed coordinate system
X, Y, Z	force components, N
L, M, N	moment components, Nm
C_X, C_Y, C_Z	axial, side, and normal force coefficients
C_l, C_m, C_n	roll, pitch, and side moment coefficients
C_{m_q}	pitch damping moment coefficient
C_{l_p}	roll damping moment coefficient

CP^R	radial center-of-pressure, calibers
CP^X	axial center-of-pressure, calibers
CG_N	center-of-gravity, calibers
N	number
δ	deflection, rad
$\vec{V}_{CG/I} = [u \quad v \quad w]^T$	velocity of projectile center-of-gravity, m/s
$\vec{\omega}_{B/I} = [p \quad q \quad r]^T$	angular velocity of projectile, rad/s
\vec{T}_{BM_i}	transformation matrix from body frame to i^{th} lifting surface frame
t	time, s
W, F, G, H	conservative variables, inviscid flux vector, viscous flux vector, source term
V, A	cell volume, cell area
subscripts i	i^{th} lifting surface
0, 1, 2, 3, 5	zeroth, first, second, third, fifth order terms
M	maneuver surface, measurement

1 DEFENSE TECHNICAL
(PDF) INFORMATION CTR
DTIC OCA

2 DIRECTOR
(PDF) US ARMY RESEARCH LAB
RDRL CIO LL
IMAL HRA MAIL & RECORDS
MGMT

1 GOVT PRINTG OFC
(PDF) A MALHOTRA

2 DIR USARL
(PDF) RDRL WML E
J SAHU
F FRESCONI

INTENTIONALLY LEFT BLANK.